Coupled maps: An approach to spatiotemporal chaos

Dimitris Stassinopoulos
University of Oxford, 1 Keble Road, Oxford OX1 3NP, United Kingdom

Preben Alstrøm
Physics Laboratory, H.C. Ørsted Institute, Universitetsparken 5, DK-2100 Copenhagen Ø, Denmark
(Received 15 May 1991)

The transition regime from periodic and quasiperiodic motion to spatiotemporal chaos is examined for coupled-map lattices. For periodic states the stability criteria for homogeneous solutions are determined, and the formation of checkerboard patterns is treated analytically. Also, the period-doubling route to spatiotemporal chaos is discussed. For the quasiperiodic transition, renormalization-group analysis is carried out for both forward coupling and the more generic linear coupling. This leads to scaling results for the spatiotemporal intermittent regime. In particular, a coherence length is identified, based on the distributions of the phase fluctuations and their derivatives. Finally, percolation methods in the study of spatiotemporal intermittency are numerically tested. It is shown that finite-size effects are substantial.

PACS number(s): 05.45.+b, 47.20.Tg, 47.25.Ae

I. INTRODUCTION

A. Spatiotemporal chaos, spatiotemporal intermittency, and weak turbulence

Chaos is a ubiquitous phenomenon widely observed in dynamical systems with a sufficient degree of nonlinearity. If, in addition, the system considered is spatially extended with effectively many degrees of freedom, we use the term *spatiotemporal chaos.* Spatiotemporal chaos is observed in a wide range of systems, particularly hydrodynamical systems (Rayleigh-Bénard convection [1,2], surface waves [3], boundary-layer flows [4]).

For the analysis of spatiotemporal chaos, two major fields in physics are applied, statistical physics and nonlinear dynamics. Statistical physics involves systems with many degrees of freedom, for example, disordered systems with (typically) an inherent degree of randomness. In contrast, nonlinear dynamics mostly has been used to describe chaos in systems with a few degrees of freedom. The motivation for the adoption of this dual scheme is the very nature of the phenomenon at hand; one cannot separate the spatial and temporal behavior—to understand the patterns formed one must understand the dynamics that created them.

A situation of particular interest is where a system by tuning an external parameter across a certain critical value effectively changes from being "low dimensional" with few degrees of freedom, and becomes "high dimensional" with many degrees of freedom. As we shall see such a transition is often followed by a breakdown of global spatial coherence. However, a macroscopic *coherence length*— a length scale below which the patterns appear coherent—may still be observed. Patterns are formed with coherent regions moving around in time and space. This complex evolution that appears right above the transition to spatiotemporal chaos is often identified as *spatiotemporal intermittency.* For fluid-dynamical systems we use the term *weak turbulence.*

B. Hydrodynamical experiments

Perhaps the best way to identify the essential features of a phenomenon is through the description of actual experiments. One example is the study of weak turbulence in vertically forced surface waves by Tufillaro, Ramshankar, and Gollub [3]. A shallow rectangular container, half filled with a fluid, is put into rapid vertical oscillations. As a result of this vertical excitation, once the amplitude A becomes bigger than a certain critical value A_c, surface waves are formed. Right above A_c these waves are highly coherent and spatially ordered, but increasing the amplitude further to $A \simeq 1.1 A_c$, the global coherence of the pattern is destroyed. However, the patterns do not seem to become totally incoherent immediately—as A increases, the coherence length gets smaller until it becomes of order of the wavelength of the underlying oscillations. A weakly turbulent regime is identified just above the breakdown of global coherence.

It is interesting to see how the same essential features appear in a totally different system. Consider another experiment: Rayleigh-Bénard convection in a high aspect-ratio cylindrical cell [1] (height much smaller than the lateral dimensions). Heat is supplied from below, generating a temperature difference ΔT between the top and the bottom plate. When this difference reaches a critical value ΔT_c, convective rolls are formed. Right above ΔT_c the rolls are stable, and the whole pattern is perfectly coherent. However, when ΔT increases above $\Delta T \simeq 1.2 \Delta T_c$, the rolls start to move erratically, and the length scale on which the patterns appear coherent decreases. Again, this partly incoherent motion of the rolls is referred to as weak turbulence.

The fact that, due to the geometry of the cell, the

 © 1992 The American Physical Society

effective degrees of freedom of the system are *weakly* coupled is an essential element in the resulting loss of spatial and temporal coherence. To appreciate this, compare, for instance, the above high-aspect-ratio experiment with a more constrained, low-aspect-ratio experiment [5], where the degrees of freedom are more strongly coupled. The latter type of setup is known to generate low-dimensional chaos and maintains its spatial coherence even after the loss of temporal order.

Although little is known about the mechanisms that generate weak turbulence, the striking similarities between diverse experimental systems suggest that a universal scheme might exist. In lieu of means of adequate characterization, even the task of their classification is by no means easy. In order to supplement the picture above, consider the Rayleigh-Bénard convection in a cubic cell [4]. In this geometry, one roll is formed with the size of the cell itself. In the bulk of the flow, heat is transmitted by convection, but layers are formed at the bottom and top boundaries, where heat is transmitted by diffusion. However, increasing the temperature difference ΔT sufficiently, instabilities of these boundary layers set in, resulting in a breakdown of their globally coherent form. The coherence length appears to decrease with increasing Rayleigh number.

Despite the disparity in the systems above, at least the main features of weak turbulence seem to be universal.

(i) The signature of weak turbulence is the onset of spatiotemporal intermittency, at which point the global spatial coherence breaks down and chaotic behavior sets in. This state should be contrasted with so-called low-dimensional chaos in which the system displays incoherence only in time, while remaining perfectly coherent in space.

(ii) The weakly turbulent regime is characterized by a dominant macroscopic length scale which can, in general, be identified as the coherent length. In that respect, weak turbulence should be contrasted with fully developed turbulence where there is no predominant length scale.

(iii) Weak turbulence appears in spatially extended systems with weak coupling between the degrees of freedom.

C. Coupled maps as a laboratory system

When a phenomenon presents features independent of the specific characteristics of systems in which it appears, we have every reason to look for a universal, underlying mechanism. In the preceding section, we have argued that weak turbulence may be such a phenomenon. But what can we say about the mechanism that governs weak turbulence? All systems sustaining weak turbulence seem to have two features in common: nonlinearity and diffusion. In fluid dynamical systems described by Navier-Stokes equations, the nonlinear term is the inertial term $(\mathbf{v}\cdot\nabla)\mathbf{v}$ and the diffusive term is the viscous term $\nu\nabla^2\mathbf{v}$. The nonlinear term tends to drive the system into a chaotic state; in a turbulent fluid, it tends to drive initially neighboring elements of the fluid further apart. The diffusive term, on the other hand, opposes this tendency and acts like a spring force that couples neighboring elements of the fluid.

These arguments, however, can offer only a qualitative interpretation. To substantiate our arguments we would like to address more rigorous questions such as the question of how to quantify the observed similarities or, for that matter, the differences between the various spatiotemporal patterns. What, for example, can we say about the dependence of the coherence length on the various physical parameters of the system in question? Can we distinguish any type of universality out of this quantitative study?

The quantitative analysis presented in the subsequent sections will be done on a simple system which shows spatiotemporal intermittency: a coupled-map lattice [6–10]. This system is not chosen to simulate a particular physical system; rather the merits of such a choice are (i) to be sure that the quantitative analysis will probe the characteristics above: the nonlinearity and the diffusion; (ii) the formal simplicity of the coupled-map lattice will lend itself to simulational analysis, a process which can be much more time consuming for more realistic systems.

II. COUPLED MAPS

A. The map, the coupling, and the initial conditions

In a coupled-map lattice every lattice point $\mathbf{r}$ is associated with a *phase* $x_n(\mathbf{r})$ for which the evolution is discrete in time (here denoted by n) and is of the form

$$x_{n+1}(\mathbf{r})=f(x_n(\mathbf{r}))+Jc_n(\mathbf{r}) , \tag{2.1}$$

where

$$c_n(\mathbf{r})\equiv\sum_{\mathbf{r}'}[g(x_n(\mathbf{r}'))-g(x_n(\mathbf{r}))] . \tag{2.2}$$

The nonlinearity is introduced by the map f, usually chosen as a circle map such as the *sine map*

$$f(x)=x+\Omega-\frac{K}{2\pi}\sin(2\pi x) , \tag{2.3}$$

or the *logistic map*

$$f(x)=Kx(1-x) . \tag{2.4}$$

In both cases, K is the nonlinearity parameter. For the circle map, Ω is a driving term; in the absence of the nonlinear term ($K=0$), Ω determines the rate of increase of the individual phases. The last term in (2.1) represents the diffusion. J is a coupling constant, and g is a coupling function. Usually, $g(x)=x$ (linear coupling), or $g(x)=f(x)$ (forward coupling), and the sum in (2.2) is restricted to nearest neighbors $\mathbf{r}'$ to lattice point $\mathbf{r}$. Notice that $c_n(\mathbf{r})$ is then the discrete Laplacian ∇^2 of $g(x_n(\mathbf{r}))$.

In all subsequent studies periodic boundary conditions are assumed, and the system evolves from a random initial configuration of the phases. We shall see that the range $[0,h]$ within which the random values for the phases are chosen can be of importance. Bearing on the analogy with thermodynamical systems we shall use the term *heat* when referring to the parameter h.

We notice that the temporal discreteness allows for faster computation of the dynamics since no explicit integration is required as is the case for simulations of

differential equations. This has proven to be an invaluable feature for real-time studies, for example, when looking at time scales, periodicities, and long transient effects.

B. Rotation number for circle maps

A quantity of central importance in the study of the dynamics of circle maps is the rotation number R, which describes the average rate of change of the phase $x(\mathbf{r})$,

$$R \equiv \lim_{n\to\infty} \left[\frac{x_n(\mathbf{r}) - x_0(\mathbf{r})}{n} \right] . \tag{2.5}$$

For the sine map (2.3) [$J=0$], one observes *mode-locked* regions in the parameter space (Ω,K) regions in which the rotation number is constant and rational [11]. As K increases, these regions (called Arnold tongues) become wider. Above $K=1$, the period-doubling route to chaos is encountered (Sec. III). When the rotation number is irrational, the evolution is quasiperiodic below $K=1$ and chaotic above (Sec. IV). Above $K=1$, the rotation number generally depends on the initial conditions.

Now, consider the coupled-sine-map lattice (2.1)–(2.3) with linear coupling [$g(x)=x$]. This system is found to have a rotation number that is *independent* of $\mathbf{r}$. The linear coupling gives rise to a springlike force between the elements of the system that prohibits the existence of different rotation numbers in the same system: a situation in which some of the phases lag behind results in big increases in the corresponding spring forces and thus a large accumulation of "potential" energy in the system; the system avoids the development of these high-energy states by synchronizing the average rate of increase of the individual phases.

For $K \leq 1$, the evolution where all phases are identical, $x_n(\mathbf{r})=x_n$, is stable, hence the dynamics reduces to the dynamics for one sine map, and is, therefore, independent of J. For $K > 1$ the shape of the Arnold tongues *does* depend on J; as J increases the mode-locked regions shrink in size. Figure 1 shows the phase diagram obtained numerically for a two-dimensional sine-map lattice with $J=0.01$, $0.5 \leq \Omega \leq 0.7$, and $1 \leq K \leq 3$. The largest Arnold tongues are shown. While the rotation number of a single sine map is known to depend on the initial conditions, the rotation number for the coupled-map lattice is found to be *independent* thereof. In this respect R, defined by (2.5) for an arbitrary lattice element, characterizes the whole system. Also shown in Fig. 1 is the path where R equals the *golden mean* $R = R_g \equiv (\sqrt{5}-1)/2$.

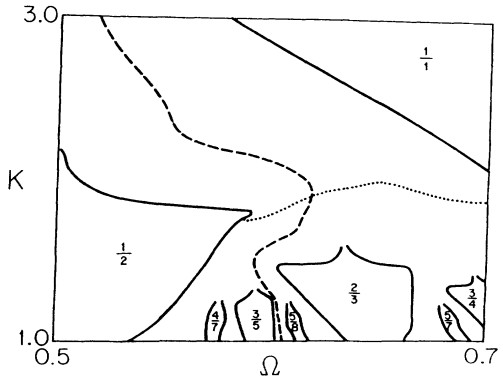

FIG. 1. Phase diagram for the coupled set of circle maps given by Eqs. (2.1)–(2.3) with $g(x)=x$ and $J=0.01$. — — —, $R=R_g$; (· · · ·), $p=0.5$.

C. Phase fluctuations

Quantities such as the rotation number are capable of probing only the overall temporal behavior of the coupled-map lattice. The many degrees of freedom in space have a profound effect on the way the system arranges its phases $x_n(\mathbf{r})$ over space. To quantify these phase arrangements we consider the *phase fluctuations* $y_n(\mathbf{r})$, defined as the difference from the average phase

$$y_n(\mathbf{r}) \equiv x_n(\mathbf{r}) - \langle x_n(\mathbf{r}') \rangle , \tag{2.6}$$

where $\langle\ \rangle$ denotes the spatial average. There are various ways the patterns formed by these fluctuations can be categorized. Here, we consider three clearly distinguishably states of the coupled-map lattice.

(i) Homogeneous states. There is no spatial difference between the phases $x_n(\mathbf{r})=x_n$ and $y_n(\mathbf{r})=0$. The dynamics of the system is effectively one dimensional.

(ii) Nonhomogeneous and spatially coherent states. The spatial differences between the phases are nonzero, but the patterns remain spatially coherent. In Sec. III, we shall particularly consider the patterns falling in this category that are periodic in time, emerging along the period-doubling route to spatiotemporal chaos.

(iii) Spatiotemporal chaotic states. The patterns are spatially incoherent and temporally chaotic. In the presence of a macroscopic coherence length, on which length-scale well-defined coherent "laminar" regions interrupted by "turbulent" behavior evolve in space and time, we use the term *spatiotemporal intermittency.* In Sec. IV, spatiotemporal intermittency is shown to emerge at the transition from quasiperiodicity to chaos. The use of percolation models in the study of spatiotemporal chaos is discussed in Sec. V.

III. PERIOD-DOUBLING ROUTE TO SPATIOTEMPORAL CHAOS

A. Transition from homogeneous to nonhomogeneous states

The period-doubling cascade is well known from studies of the logistic map (2.4) [12]. Increasing the value of K above $K=3$, the fixed point solution $x_n=(K-1)/K$ is no longer stable; instead the dynamics drives the phase towards a cyclic behavior $x_1,x_2,x_1,\ldots$ of period 2. Increasing the value of K further, other period doublings follow, increasing the period of the cycle by a factor of 2 every time. At a critical K value, $K=K_c$ ($K_c=3.5699\ldots$), the cycle length diverges, and K_c is identified as a transition point to chaos.

For the circle map, period doublings appear inside the Arnold tongues. For small values of the nonlinearity K, a mode-locked region with rotation number $R=P/Q$ is

characterized by a stable periodic motion of period Q. However, a sufficient increase of K destabilizes this motion, and the phase drives into a periodic motion with a period twice as large.

For coupled-map lattices, period doublings are also observed. A main question is here how the coupling and the possibility of a spatial distribution of phases affects these transitions. How do phase configurations change as we increase the nonlinearity parameter K of the system? Consider first the forward coupling ($g=f$). Then the nonlinearity and the coupling can be separated [13],

$$x_{n+1}(\mathbf{r})=Mf(x_n(\mathbf{r}))\ , \tag{3.1}$$

where

$$M=1+J\nabla^2\ . \tag{3.2}$$

For the sake of simplicity, we have used the continuous space formulation, replacing $c_n(\mathbf{r})$ by $\nabla^2 g(x_n(\mathbf{r}))$. M and f commute for a small perturbation $\delta x(\mathbf{r})$ of the homogeneous state $x(\mathbf{r})=x_0$,

$$\begin{aligned} Mf(x_0+\delta x(\mathbf{r}))&\simeq(1+J\nabla^2)[f(x_0)+f'(x_0)\delta x(\mathbf{r})]\\ &=f(x_0)+f'(x_0)(1+J\nabla^2)\delta x(\mathbf{r})\\ &\simeq fM[x_0+\delta x(\mathbf{r})]\ . \end{aligned} \tag{3.3}$$

After N iterations, the perturbation $\delta x_N(\mathbf{r})$ from the homogeneous state $x_N=f^N(x_0)$ is

$$\delta x_N(\mathbf{r})\simeq\Lambda_N M^N\delta x(\mathbf{r})\ , \tag{3.4}$$

where

$$\Lambda_N\equiv\prod_{n=0}^{N-1}f'(x_n) \tag{3.5}$$

determines the stability of the orbit $\{x_n=f^n(x_0)\}$ for $J=0$ (if $\Lambda_N\to 0$ when $N\to\infty$, the orbit is stable).

Consider the Fourier expansion of the perturbation $\delta x(\mathbf{r})$,

$$\delta x(\mathbf{r})=\sum_q \delta x_q e^{i\mathbf{q}\cdot\mathbf{r}}\ . \tag{3.6}$$

Since

$$Me^{i\mathbf{q}\cdot\mathbf{r}}=(1-Jq^2)e^{i\mathbf{q}\cdot\mathbf{r}}\ , \tag{3.7}$$

the amplitude $\delta x_{N,\mathbf{q}}$ of the term $e^{i\mathbf{q}\cdot\mathbf{r}}$ after N iterations is

$$\delta x_{N,\mathbf{q}}\simeq\Lambda_N(1-Jq^2)^N\delta x_{\mathbf{q}}\ . \tag{3.8}$$

Thus all stable orbits for the single map ($J=0$) remain stable in the corresponding homogeneous state when forward coupling is applied.

The homogeneous states of stable single-map orbits are not stable in general. To see this, consider the linear coupling

$$x_{n+1}(\mathbf{r})=(f+J\nabla^2)x_n(\mathbf{r})\ . \tag{3.9}$$

For a small perturbation $\delta x(\mathbf{r})$ to the homogeneous state $x(\mathbf{r})=x_0$, we have

$$(f+J\nabla^2)[x_0+\delta x(\mathbf{r})]\simeq f(x_0)+[f'(x_0)+J\nabla^2]\delta x(\mathbf{r})\ . \tag{3.10}$$

After N iterations the perturbation is

$$\delta x_N(\mathbf{r})\simeq[f'(x_{N-1})+J\nabla^2]\cdots[f'(x_0)+J\nabla^2]\delta x(\mathbf{r})\ . \tag{3.11}$$

The corresponding Fourier amplitudes $\delta x_{N,\mathbf{q}}$ are

$$\delta x_{N,\mathbf{q}}\simeq\prod_{n=0}^{N-1}[f'(x_n)-Jq^2]\delta x_{\mathbf{q}}\ . \tag{3.12}$$

To lowest order in q, (3.12) yields

$$\delta x_{N,\mathbf{q}}\simeq\Lambda_N\left(1-\sum_{n=0}^{N-1}[f'(x_n)]^{-1}Jq^2\right)\delta x_{\mathbf{q}}\ . \tag{3.13a}$$

If the single-map orbit is *superstable*, i.e., if one of the derivatives is zero, say $f'(x_0)=0$, (3.13a) is replaced by

$$\delta x_{N,\mathbf{q}}\simeq-\left[\prod_{n=1}^{N-1}f'(x_n)\right]Jq^2\delta x_{\mathbf{q}}\ . \tag{3.13b}$$

Thus only when the sum in (3.13a) is *positive*, the linear coupling increases the stability of the orbit. When the sum is *negative*, the stability decreases, and the system is most unstable to *short* wavelengths (large q values); hence the lowest-order approximation (3.13) is of doubtful value.

As an example, consider the sine-map lattice (2.1)–(2.3) with linear coupling and Ω chosen inside an Arnold tongue. By (3.12) the stability criterion for the homogeneous solution is

$$\Lambda(K,Jq^2)\equiv\left|\prod_{n=0}^{Q-1}(1-K\cos 2\pi x_n-Jq^2)\right|<1\ , \tag{3.14}$$

when the rotation number is $R=P/Q$. Figure 2 shows the function $\Lambda(K=1,Jq^2)$ for $J=0.01$ and for various rotation numbers at the superstable-orbit value of Ω (where $x_0=0$). It is noted that for larger Q values, the maximum

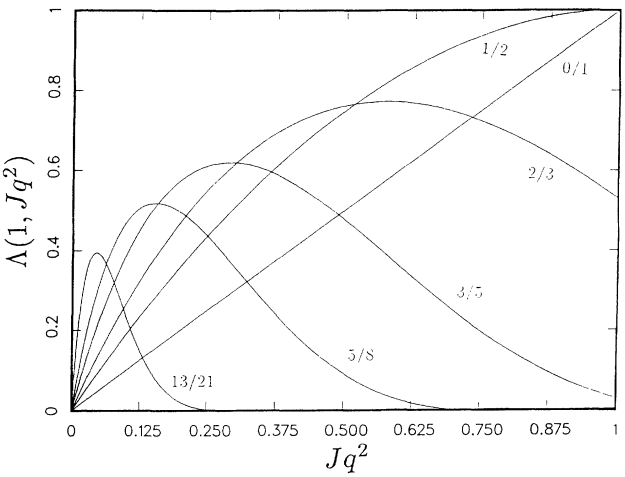

FIG. 2. $\Lambda(1,Jq^2)=Jq^2|\prod_{n=1}^{Q-1}(1-\cos 2\pi x_n-Jq^2)|$ as a function of Jq^2 for the Arnold tongues corresponding to rotation numbers $\frac{0}{1}$, $\frac{1}{2}$, $\frac{2}{3}$, $\frac{3}{5}$, $\frac{5}{8}$ and $\frac{13}{21}$, where Ω is chosen such that $x_0=0$.

value of $\Lambda(1,Jq^2)$ shifts to smaller wave numbers (larger wavelengths), i.e., the destabilizing wavelength increases with Q.

Numerical studies at the breakdown of the homogeneous state confirm the conclusions above. On a square lattice the shortest wavelength is 2 (lattice units). In accordance with this, a transition from a homogeneous state to a nonhomogeneous *checkerboard* state has been observed in simulations for both the logistic-map [6(b)] and the sine-map lattice for $P/Q=\frac{1}{2}$ (Fig. 3, see below). For the logistic-map lattice a detailed description of the checkerboard bifurcation structure, including the effects of longer-wavelength instabilities, can be found in Ref. [6b]. For the sine-map lattice Fig. 4 shows the wave pattern obtained for $P/Q=\frac{13}{21}$ and $J=0.1$. The wavelength observed agrees well with the wavelength about 9 calculated from the value $Jq^2\simeq 0.05$ at which $\Lambda(1,Jq^2)$ is maximal (Fig. 2).

Next, we consider in detail the scenario for the sine-map lattice with linear coupling along the path $\Omega=\frac{1}{2}$ located inside the $R=\frac{1}{2}$ Arnold tongue. First, assume that

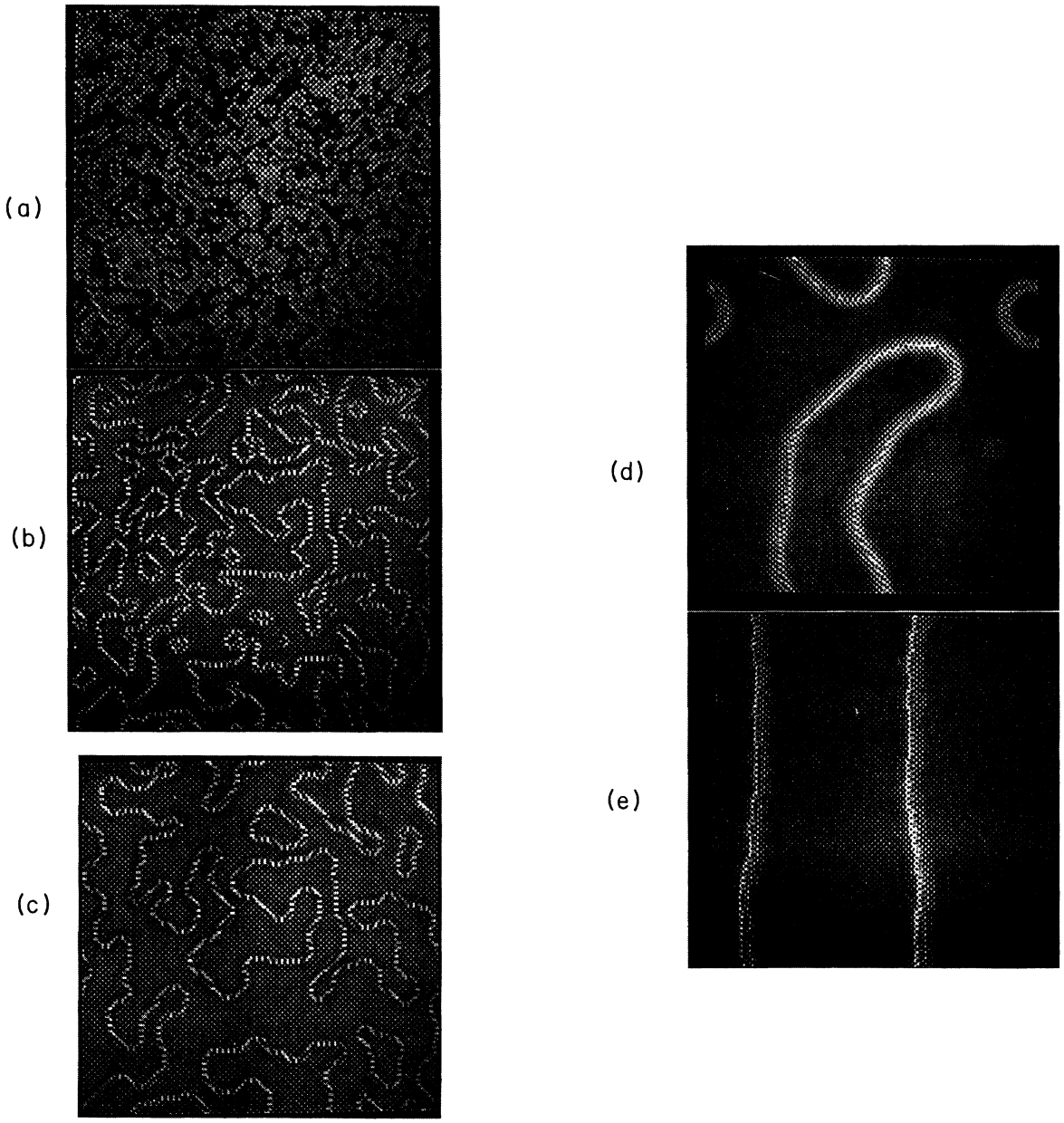

FIG. 3. (a)–(c) Checkerboard evolution for a 128×128 system at $K=1.380$ and $J=0.01$. (a) 150 time steps. (b) 500 time steps. (c) 2000 time steps. (d)–(e) Two distinct checkerboard states for a 128×128 system at $K=1.025$ and $J=0.1$. (d) 3000 iterations. The loops will eventually disappear after $\sim70\,000$ iterations. (e) The same system started from different initial conditions after 100 000 iterations. The domain walls will remain.

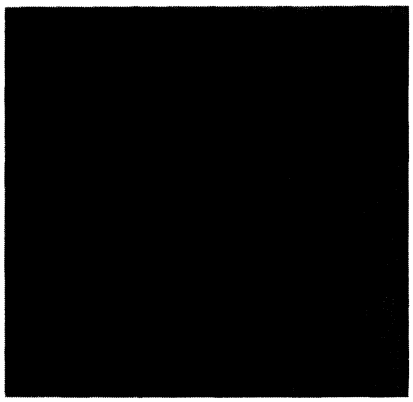

FIG. 4. A snapshot for a 128×128 system at $K=1.048\,95$ and $J=0.1$ along the $\frac{13}{21}$ Arnold tongue.

the system is in the regime where it can sustain the homogeneous solution with all lattice points undergoing the same period two orbit $\{0,\frac{1}{2},1,\frac{3}{2},\dots\}$ [14]. In the continuous-space formulation, the stability is determined by the condition

$$\Lambda(K,Jq^2)\equiv|[f'(\tfrac{1}{2})-Jq^2][f'(0)-Jq^2]| =|(1+K-Jq^2)(1-K-Jq^2)|<1 . \quad (3.15)$$

For $0<Jq^2<2$, the homogeneous solution is stable when $|K|<K_q$, where

$$K_q=[(1-Jq^2)^2+1]^{1/2} . \quad (3.16)$$

What is important to point out here is the fact that K_q *decreases* from the single-map period-doubling point $K_0=\sqrt{2}$ when q increases, i.e., the smaller the wavelength, the smaller is the value of K_q, indicating that the homogeneous state first becomes unstable to the shortest wavelengths. The shortest wavelength (2 lattice units) corresponds to $q=\pi$, which gives an estimate of the point of instability; for $J=0.01$, for example, (3.16) gives $K_\pi\simeq1.3462\dots$.

In accordance with the analysis above, numerical simulations on a square lattice show that checkerboard patterns are formed when the homogeneous period-2 state breaks down (Fig. 3). To find the accurate value for the point of breakdown, $K=K_1$, we therefore consider a "checkerboard perturbation" to the homogeneous period-2 orbit, now taking into account the discreteness of the lattice. Writing $\mathbf{r}=(i,j)$, we have

$$c_n(i,j)\equiv\sum_{\langle k,l\rangle}[x_n(k,l)-x_n(i,j)] , \quad (3.17)$$

where $\langle k,l\rangle$ means the set of four nearest neighbors to lattice point (i,j). A checkerboard perturbation has the form

$$\delta x(i,j)=\begin{cases}\delta x_a & \text{if } i+j \text{ is even}\\ \delta x_b & \text{if } i+j \text{ is odd} .\end{cases} \quad (3.18a)$$

The symmetry of the dynamics ensures that the perturbation remains a checkerboard after N iterations,

$$\delta x_N(i,j)=\begin{cases}\delta x_{N,a} & \text{if } i+j \text{ is even}\\ \delta x_{N,b} & \text{if } i+j \text{ is odd} .\end{cases} \quad (3.18b)$$

From the initial state $x_0(i,j)=\delta x(i,j)$ (perturbed from the homogeneous state $x_0=0$), we have by iteration ($i+j$ even)

$$x_1(i,j)=f(\delta x_a)+Jc_0(i,j) \simeq f(0)+[f'(0)-4J]\delta x_a+4J\delta x_b . \quad (3.19)$$

Hence

$$\delta x_{1,a}\simeq[f'(0)-4J]\delta x_a+4J\delta x_b . \quad (3.20a)$$

Similarly, $\delta x_{1,b}$ is found to be

$$\delta x_{1,b}\simeq[f'(0)-4J]\delta x_b+4J\delta x_a . \quad (3.20b)$$

Alternatively, (3.20) can be written in matrix form,

$$\begin{bmatrix}\delta x_{1,a}\\ \delta x_{1,b}\end{bmatrix}\simeq\begin{bmatrix}B(0) & 4J\\ 4J & B(0)\end{bmatrix}\begin{bmatrix}\delta x_a\\ \delta x_b\end{bmatrix} , \quad (3.21)$$

where

$$B(x)\equiv f'(x)-4J=1-K\cos2\pi x-4J . \quad (3.22)$$

Further iteration from the state $x_1(i,j)=\frac{1}{2}+\delta x_1(i,j)$ yields

$$\begin{bmatrix}\delta x_{2,a}\\ \delta x_{2,b}\end{bmatrix}\simeq\begin{bmatrix}B(\frac{1}{2}) & 4J\\ 4J & B(\frac{1}{2})\end{bmatrix}\begin{bmatrix}B(0) & 4J\\ 4J & B(0)\end{bmatrix}\begin{bmatrix}\delta x_a\\ \delta x_b\end{bmatrix} . \quad (3..23)$$

We write

$$\begin{bmatrix}\delta x_{2,a}\\ \delta x_{2,b}\end{bmatrix}\simeq\underline{A}\begin{bmatrix}\delta x_a\\ \delta x_b\end{bmatrix} , \quad (3.24a)$$

where

$$\underline{A}\equiv\begin{bmatrix}B(\frac{1}{2})B(0)+16J^2 & 4J[B(\frac{1}{2})+B(0)]\\ 4J[B(\frac{1}{2})+B(0)] & B(\frac{1}{2})B(0)+16J^2\end{bmatrix} . \quad (3.24b)$$

by (3.22), $B(0)=1-K-4J$ and $B(\frac{1}{2})=1+K-4J$. Hence

$$\underline{A}=\begin{bmatrix}1-K^2-8J(1-4J) & 8J(1-4J)\\ 8J(1-4J) & 1-K^2-8J(1-4J)\end{bmatrix} . \quad (3.25)$$

In general, we have

$$\begin{bmatrix}\delta x_{2N,a}\\ \delta x_{2N,b}\end{bmatrix}\simeq\underline{A}^N\begin{bmatrix}\delta x_a\\ \delta x_b\end{bmatrix} . \quad (3.26)$$

Thus the stability criterion is

$$\max\{|\lambda_i|\}<1 \quad (i=1,2) , \quad (3.27)$$

where

$$\lambda_1=1-K^2, \quad \lambda_2=1-K^2-16J(1-4J) \quad (3.28)$$

are the eigenvalues of the matrix $\underline{A}$. In analogy with (3.16), we get (for $0<J<\frac{1}{4}$) the stability condition $|K|<K_1$, where

$$K_1=[(1-8J)^2+1]^{1/2} . \tag{3.29}$$

Note the good estimate that (3.16) gave for K_1.

Direct substitution into (3.29) gives $K_1=1.358\,823...$ for $J=0.01$ and $K_1=1.019\,803...$ for $J=0.1$. Based on the above arguments that the discrete homogeneous state is mostly unstable to checkerboard perturbations, K_1 equals the *lowest* transition point from a homogeneous to a nonhomogeneous state. In order to identify this transition, we consider the distribution $D(y)$ in space and time of the phase fluctuations $y_n(\mathbf{r})$ [Eq. (2.6)]. The width w of $D(y)$ is defined by

$$w\equiv\{\langle\langle[y_n(\mathbf{r})]^2\rangle\rangle\}^{1/2} , \tag{3.30}$$

where $\langle\langle\ \rangle\rangle$ denotes the average over space *and* time. In Fig. 5, w (determined from numerical simulations) is shown as a function of $K-K_1$ for both $J=0.01$ and $J=0.1$. The linear behavior in Fig. 5 shows that

$$w\sim(K-K_1)^{\beta} , \tag{3.31}$$

where β is determined by the slope, in both cases $\beta=0.500\pm0.001$. We conclude that the first transition from homogeneous to nonhomogeneous solutions can be described as a "second-order" phase transition with associated "order parameter" w, and "order parameter" exponent β. The transition point is found to be $K=K_1\pm0.000\,05$. The results provide strong evidence that K_1 is the *lowest* transition point from a homogeneous to a nonhomogeneous state.

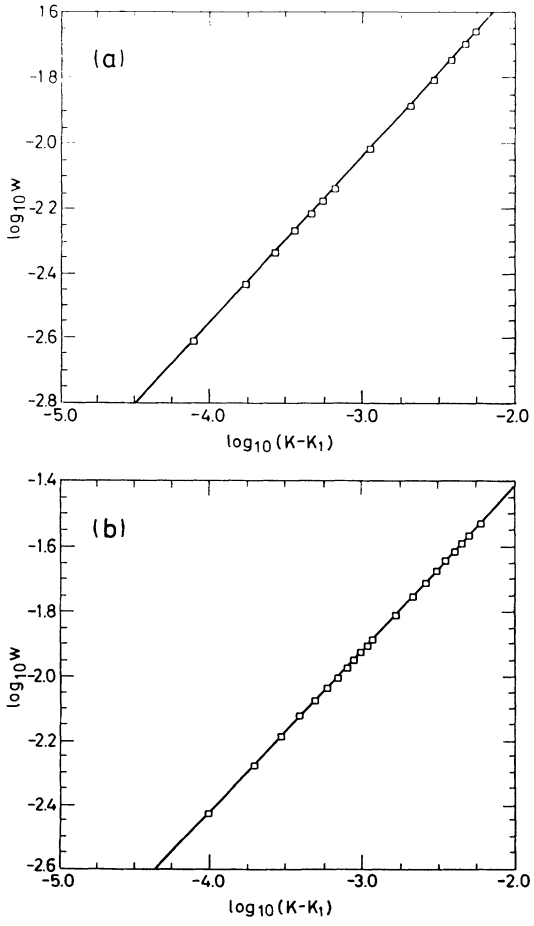

FIG. 5. Logarithmic plot of w vs $K-K_1$ ($h=0.3$). (a) $J=0.01$, $K_1=1.358\,82$. (b) $J=0.1$, $K_1=1.019\,80$. In both cases, the slope is $\beta=0.500\pm0.001$.

Numerical simulations show that when the homogeneity breaks down, the period doubles from 2 to 4. This observation gives another way to determine K_1, but more importantly, it gives an explanation to the result $\beta=\frac{1}{2}$: By symmetry, the checkerboard structure has the form $(\delta x_a,\delta x_b)=(\epsilon,-\epsilon)$. Expanding to third order, we find for the second iterate ($\delta x_{2,b}=-\delta x_{2,a}$)

$$\delta x_{2,a}\simeq\lambda_2\epsilon+\psi(J,K)\epsilon^3 , \tag{3.32}$$

where

$$\psi(J,K)\equiv[(1-4J)^2+\tfrac{1}{3}K^2](2\pi K)^2 . \tag{3.33}$$

For the period-4 solution $(\delta x_{2,a},\delta x_{2,b})=(-\epsilon,\epsilon)$. By (3.28) and (3.29), we have $-(1+\lambda_2)=K^2-K_1^2$, and (3.32) yields ($K\simeq K_1$)

$$\epsilon^2\simeq\frac{K^2-K_1^2}{\psi(J,K)}\simeq\frac{2K_1}{\psi(J,K_1)}(K-K_1) . \tag{3.34}$$

Thus $w\sim\epsilon\sim(K-K_1)^{1/2}$ and $\beta=\frac{1}{2}$.

B. Checkerboard-state evolution

The above discussion, based on stability analysis, focused only on the tendency of the sine-map lattice (2.1)–(2.3) to build up checkerboard structures when the value of K was larger than a certain value K_1. However, this will not always happen. The reason is that the system, due to the diffusive term, has the tendency to smooth out the perturbations [15]. These two tendencies of the system compete—the smoothing process winning at large perturbation wavelengths, and the checkerboard-building process winning at small wavelengths. The competition gives rise to transient stages of evolution with nucleation of checkerboard patterns [16]. We will demonstrate the two tendencies in a more quantitative way. As a measure of the perturbation we use the heat h (amplitude of the random initial state).

To illustrate the tendency of the system to follow each of the two above-mentioned processes, we have in Fig. 6 sketched the characteristic times, i.e., the time it takes for each process to develop assuming that the other process is in a latent state, as a function of the heat h [17]. For the smoothing process the characteristic time, denoted by $\tau^{(s)}$, is zero when the heat is zero, and it increases as the heat increases [18]. For the checkerboard-building process the characteristic time is infinite when the heat is zero—in the absence of perturbations the system will remain homogeneous. As the heat increases, the characteristic time decreases [19]. This process is described by a family of lines $\tau^{(c)}(K)$, one for each K, with the top line $\tau_1^{(c)}$ corresponding to the value K_1 for which a checkerboard pattern is marginally formed, and with the lower ones corresponding to higher values of the nonlinearity

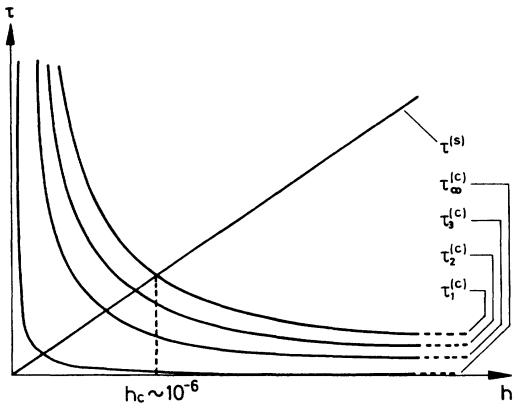

FIG. 6. Schematic representation of the characteristic time for the smoothing process $\tau^{(s)}$ and the checkerboard-building process $\tau^{(c)}$ as a function of the "heat" h. The family of curves $\tau_1^{(c)}, \tau_2^{(c)}, \ldots$, indicates the dependence of the checkerboard-building process on K. The upper member of the family $\tau_1^{(c)}$ corresponds to $K = K_1$ where the checkerboard structure is barely formed. The lowest one $\tau_\infty^{(c)}$ corresponds to $K_\infty = \sqrt{2}$. This is the case where the checkerboard process dominates even for infinitesimally small values of h.

parameter. The lowest one $\tau_\infty^{(c)}$ corresponds to $K_\infty = \sqrt{2}$. This is the case where the checkerboard process dominates even for infinitesimally small values of h. The point of intersection between $\tau_1^{(c)}$ and $\tau^{(s)}$ defines a critical value h_c for the heat.

For values of the heat above h_c, $\tau_1^{(c)} < \tau^{(s)}$, and therefore checkerboard structures form at K_1. But for a value $h = h'$ of the heat below h_c, $\tau_1^{(c)} > \tau^{(s)}$, and in order for the checkerboard process to prevail, we have to increase the value of the nonlinearity parameter K further, namely to a value $K = K'$, at which the corresponding characteristic time $\tau'^{(c)}$ equals $\tau^{(s)}$ at $h = h'$. Numerically h_c has been found to be $\sim 10^{-6}$.

To demonstrate the difference between the way the sine-map system crosses over to checkerboard patterns above and below h_c, the width w of the fluctuation distribution [cf. (3.30)] is plotted as a function of K for three different values of the heat h (Fig. 7). Numerically, the width w is found to be a well-defined function of h, independently of the specific initial state. Note the jump from the homogeneous state to the checkerboard state when the heat is smaller than h_c.

In Fig. 3 a sequence of pictures is shown, displaying the transient stages prior to the formation of a checkerboard pattern. The nucleationlike nature of the process is apparent. What happens is the following: The initial white noise is smoothed out by the diffusion term [15]. At the same time the system starts to rearrange itself into checkerboard structures. Throughout the system centers of checkerboard-formation activity appear and start to spread [Fig. 3(a)]. This is a local process and it happens faster wherever the initial configuration is a favorable one. If the characteristic time of the checkerboard-formation process is shorter than that of the smoothing process, eventually the checkerboard formations will spread and cover the whole lattice. In Fig. 3b, the state is shown for the same parameter values at a time where the isolated checkerboard domains have started to merge. Because two adjacent domains can be out of phase, they will not merge but instead relax the frustration by developing a domain wall [6b]. In the beginning these domain walls appear interwoven, but in the course of time they smooth out [Fig. 3(c)]. Eventually, two things can happen: either the one phase will completely dominate [perfect checkerboard, Fig. 3(d)], or both phases will coexist separated by a domain wall [Fig. 3(e), keep in mind that due to the periodic boundary conditions the planar lattice is folded into a torus].

C. Onset of spatiotemporal chaos

Finally, we give a brief survey of the pattern evolution as K increases along the $\Omega = \frac{1}{2}$ path. In Fig. 8, we look at the fluctuation width w as a function of K and h for

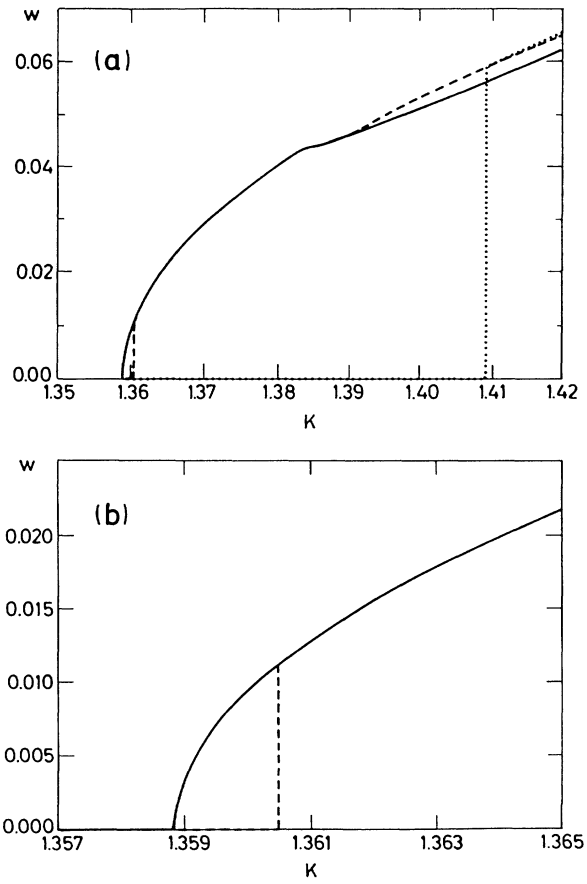

FIG. 7. Width w plotted as function of K for fixed $J=0.01$ and for different values of the heat. ——, $h = 1.0\times10^{-2}$; — — —, $h = 1.0\times10^{-10}$; · · · ·, $h = 1.0\times10^{-14}$. Notice the jump in w at the transition point $K = K'$ from homogeneous states to checkerboard structures when $h = h' < h_c$: For $h = 1.0\times10^{-2}$, $K' = K_1 = 1.3588$; for $h = 1.0\times10^{-10}$, $K' = 1.361$; and for $h = 1.0\times10^{-14}$, $K' = 1.41 \simeq \sqrt{2}$.

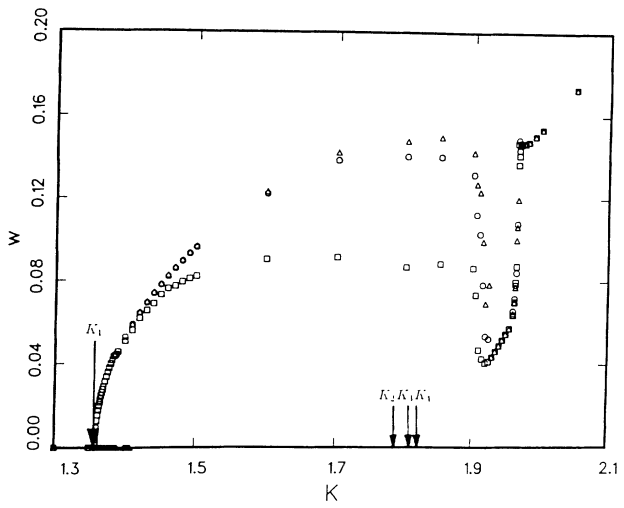

FIG. 8. Width w plotted vs K for fixed $J=0.01$, and for different values of the heat. □, $h=10^{-2}$; ○, $h=10^{-10}$; △, $h=10^{-14}$. The period-doubling points K_2, K_3, and K_4 are also indicated.

$J=0.01$. The value of w for (K,h) values leading to checkerboard patterns is *independent* of h. However, increasing K further, the value of w start to depend on h. At $K=1.5$, well below the second period-doubling point K_2, the checkerboard structures have shrunk to small regions and patterns of larger wavelength have started to dominate. We have marked the points of subsequent period doublings: $K_2=1.789$, $K_3=1.809$, $K_4=1.821$. Mere inspection of the first few members of this sequence is enough to place the accumulation point $K=K_c\simeq 1.84\pm 0.01$.

At $K=1.9$, well above the onset of chaos K_c, one still finds a checkerboardlike "background," now with many isolated points of chaotic activity on top of it. Further increase of K results in an abrupt decrease in w (Fig. 8). The patterns acquire a more complicated structure and they fluctuate less. Yet the patterns retain their spatial coherence [7]. The dip in w indicates that the disappearance of the checkerboard mode is a breakdown process—suddenly, the checkerboard mode, due to the increase of the nonlinearity, becomes unstable. Despite the fast chaotic activity, the new favorable state is flatter than before. This is due to the fact that the system is able to wander over more degrees of freedom, and therefore it can choose a smoother state. The system remains into this coherent-chaotic state [9] up to $K=1.96$. At that value the system looses the spatial coherence and crosses over to a spatiotemporal chaotic behavior. The onset to spatiotemporal chaos manifests itself as a sharp increase in w. We emphasize that w is *independent* of h in the spatiotemporal chaotic regime.

It is noted that for smaller mode-locked regions, the parameter regime between the homogeneous state and spatiotemporal chaos is smaller, and the intermediate stages become increasingly difficult to observe.

IV. QUASIPERIODIC ROUTE TO SPATIOTEMPORAL INTERMITTENCY

A. Onset of spatiotemporal intermittency

In this section we concentrate on the dynamics of the sine-map lattice (2.1)–(2.3) along an "irrational path" outside mode-locked regions, defined as the curve in (Ω,k) space along which the rotation number R is fixed and irrational. The dashed curve in Fig. 1 is the irrational path for the golden mean $R=R_g\equiv(\sqrt{5}-1)/2$. Numerical simulations along the "golden-mean path" $R=R_g$ have shown that the point $K=1$ is of special significance. Below that point the system falls into the homogeneous state, which means that our system for $K\leq 1$ is completely described by one sine map ($J=0$). The point $(\Omega,K)=(\Omega_g,1)$, where Ω_g is the Ω value for the golden mean at $K=1$, is a very special point on the golden-mean path: it is the point at which the dynamics becomes chaotic. The system is observed to change drastically. From a perfectly "flat" homogeneous state below $K=1$, the system crosses over to a nonhomogeneous state that shows all the features of spatiotemporal intermittency as described in Sec. II [Fig. 9(a)]. In particular, a macroscopic coherence length ξ is found to diverge as K approaches $K=1$ from above.

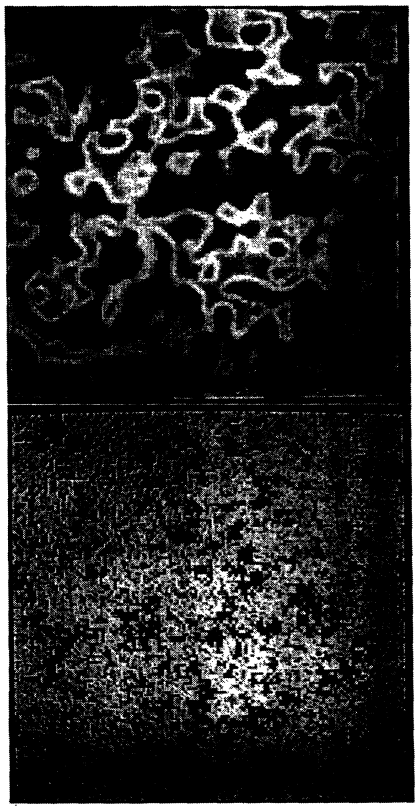

FIG. 9. Two typical spatial patterns above the onset of chaos (system size 128×128). $K=1.1$ and (a) $J=0.1$, (b) $J=0.0015$. The value of Ω is chosen such that the rotation number equals the golden mean R_g.

To describe the onset of spatiotemporal intermittency, we follow the general renormalization-group scheme [13,20]. The renormalization-group transformation T for the circle map (2.3) at the critical point $(\Omega,K)=(\Omega_g,1)$ has the form

$$\begin{bmatrix} f_{n+1}(x) \\ f_n(x) \end{bmatrix} = T \begin{bmatrix} f_n(x) \\ f_{n-1}(x) \end{bmatrix} = \begin{bmatrix} \alpha f_n(\alpha f_{n-1}(x/\alpha^2)) \\ f_n(x) \end{bmatrix} , \tag{4.1}$$

where $\alpha=-1.2885\ldots$. The fixed-point function f^* for T is given by

$$f^*(x)=\alpha f^*(\alpha f^*(x/\alpha^2)) , \tag{4.2}$$

where $f^*(0)$ is arbitrary, but usually chosen to be 1. Perturbations from f^* are studied by iterative use of T: From initial deviations $f_0=f^*+h_0$ and $f_1=f^*+h_1$, h_n is defined by

$$\begin{bmatrix} f^*+h_{n+1} \\ f^*+h_n \end{bmatrix} = T \begin{bmatrix} f^*+h_n \\ f^*+h_{n-1} \end{bmatrix} . \tag{4.3}$$

The (largest) eigenvalue μ associated with the perturbation is determined by the relation $h_n \sim \mu^n h_0$. For instance, for a small change $\epsilon=|K-1|$ in the K value, the perturbation is of the form ϵx, and $\mu=\alpha^2$ [20].

Here we are interested in perturbations of the type $J\nabla^2 g$ (J small). Based on the equality $\nabla^2 g(x+\delta x(\mathbf{r}))=g'(x)\nabla^2\delta x(\mathbf{r})$ for a small perturbation, (4.1) and (4.3) yield

$$h_n(x+\delta x(\mathbf{r}))=J_n(x)\nabla^2 g(x+\delta x(\mathbf{r})) , \tag{4.4}$$

where $J_n(x)$ is given by the recursion relation

$$\begin{aligned} g'(x)J_{n+1}(x) &= f^{*'}(x/\alpha^2)g'(\alpha f^*(x/\alpha^2))J_n(\alpha f^*(x/\alpha^2)) \\ &\quad + f^{*'}(\alpha f^*(x/\alpha^2))g'(x/\alpha^2)J_{n-1}(x/\alpha^2) . \end{aligned} \tag{4.5}$$

For the forward coupling, $g=f^*$, and by (4.2), (4.5) reduces to

$$\begin{aligned} f^{*'}(x)J_{n+1}(x) &= f^{*'}(x)[J_n(\alpha f^*(x/\alpha^2)) \\ &\quad + J_{n-1}(x/\alpha^2)] , \end{aligned} \tag{4.6}$$

with the simple solution $J_n(x)=J_n\sim A_n$, where $A_0, A_1, \ldots$ is the Fibonacci sequence, defined recursively by $A_{n+1}=A_n+A_{n-1}$, with $A_0=A_1=1$. Furthermore, $A_n\sim R_g^{-n}$, hence the relevant eigenvalue is $\mu=1/R_g=1.6180\ldots$.

If $g'(0)\neq 0$, as is the case for the linear coupling $g(x)=x$, we find, for $x=0$ [$f^{*'}(0)=0$],

$$g'(0)J_{n+1}(0)=f^{*'}(\alpha)g'(0)J_{n-1}(0) . \tag{4.7}$$

By differentiation of (4.2), one finds $f^{*'}(\alpha)=\alpha^4$. Thus (4.7) has the solution $J_n(0)\sim\alpha^{2n}$, corresponding to the eigenvalue $\mu=\alpha^2=1.6602\ldots$. Note that $\alpha^2>1/R_g$. For other initial conditions we have

$$\begin{aligned} \frac{g'(x)}{f^{*'}(x)}J_{n+1}(x) &= \frac{g'(\alpha f^*(x/\alpha^2))}{f^{*'}(\alpha f^*(x/\alpha^2))}J_n(\alpha f^*(x/\alpha^2)) \\ &\quad + \frac{g'(x/\alpha^2)}{f^{*'}(x/\alpha^2)}J_{n-1}(x/\alpha^2) . \end{aligned} \tag{4.8}$$

Repeated use of (4.8) (from initial values J_0, J_1) shows, nevertheless, that the behavior at $x=0$ eventually will dominate: For J_n there will be $A_{n-1}\, g'/f^{*'}$ terms times J_1 and $A_{n-2}\, g'/f^{*'}$ terms times J_0. Naively, one then would guess that $J_n\sim A_n$, and $\mu=1/R_g$. However, even from the last term on the right-hand side of (4.8) we have (n odd)

$$\frac{g'(x)}{f^{*'}(x)}J_{n+1}(x)=\frac{g'(x/\alpha^{n+1})}{f^{*'}(x/\alpha^{n+1})}J_0(x/\alpha^{n+1})+\cdots , \tag{4.9}$$

where the ellipses denote other terms. For small x, $f^{*'}(x)\sim x^2$, i.e., $g'(x/\alpha^{n+1})/f^{*'}(x/\alpha^{n+1})\sim\alpha^{2(n+1)}$. Hence $\mu=\alpha^2$ or larger.

A closer inspection of the actual x values entering the $g'(x)/f^{*'}(x)$ terms shows that these can be divided into $(n-1)/2$ groups G_m, where G_m contains A_{2m} elements of order α^{2m-n}. To illustrate this, consider $x=\alpha^{-1}$ in (4.8). This gives a value $\alpha f^*(x/\alpha^2)\simeq\alpha$ on level n, and a value $x/\alpha^2=\alpha^{-3}$ on level $n-1$. The value α on level n gives a value $\alpha f^*(\alpha^{-1})=\alpha^{-1}$ on both level $n-1$ and $n-2$, while α^{-3} on level $n-1$ gives $\alpha f^*(\alpha^{-5})\simeq\alpha$ on level $n-2$ and α^{-5} on level $n-3$. The point is that all the values entering are of the form α^{-k}, where $k\geq -1$ is odd. The rest is trivial counting (for simplicity, $k=-1$ and 1 form one group). In the above notation, the corresponding $g'/f^{*'}$ terms are of order α^{2n-4m}, and the eigenvalue can be found,

$$J_n\sim\sum_m A_{xm}\alpha^{2n-4m}\sim\alpha^{2n} , \tag{4.10}$$

since $A_{2m}\sim R_g^{-2m}$ and $\alpha^2 R_g>1$. Hence $\mu=\alpha^2$.

From the analysis above, we see that using forward coupling $g=f$, we move in a very special direction in function space—a direction with a smaller eigenvalue ($1/R_g$) than the dominant one α^2. This is also the case for the transition to spatiotemporal intermittency at other rotation numbers. Consider, e.g., the rotation numbers $R(n)=\lim_{m\to\infty}A_m(n)/A_{m+1}(n)$, where $A_{m+1}(n)=nA_m(n)+A_{m-1}(n)$ ($n=1$ is the golden mean). For forward coupling, the eigenvalue obtained is $1/R(n)$, while for the linear coupling, one obtains the eigenvalue $[\alpha(n)]^2$, where $\alpha(n)$ is the associated single-map scaling factor. We can compare the two eigenvalues by writing $|\alpha(n)|=[1/R(n)]^{x(n)}$; then the largest eigenvalue is $[\alpha(n)]^2$ if $x(n)>0.5$ and $1/R(n)$ if $x(n)<0.5$. A careful analysis shows that $x(n)$ decreases with n [20(a),21] from the value $x(1)=0.527\ldots$. At $n=5$, $x(n)$ barely becomes smaller than 0.5, $x(5)=0.496\ldots$.

An analysis similar to that above can be made for coupled logistic maps [22]. In that case, the renormalization-group transformation T is

$$f_{n+1}(x)=T[f_n(x)]=\alpha f_n^2(x/\alpha) , \tag{4.11}$$

where $\alpha=-2.5028\ldots$, and the fixed-point function f^* is given by

$$f^*(x)=\alpha f^{*2}(x/\alpha)\ . \tag{4.12}$$

Then, (4.5) is replaced by

$$g'(x)J_{n+1}(x)=f^{*'}(x/\alpha)g'(f^*(x/\alpha))J_n(f^*(x/\alpha)) + f^{*'}(f^*(x/\alpha))g'(x/\alpha)J_n(x/\alpha)\ . \tag{4.13}$$

For $g=f^*$, we have

$$f^{*'}(x)J_{n+1}(x)=f^{*'}(x)[J_n(f^*(x/\alpha))+J_n(x/\alpha)]\ , \tag{4.14}$$

with the solution $J_n(x)=J_n\sim 2^n$, and eigenvalue [13] $\mu=2$. When $g'(0)\neq 0$, $x=0$ yields

$$g'(0)J_{n+1}(0)=f^{*'}(1)g'(0)J_n(0)\ . \tag{4.15}$$

Differentiation of (4.12) gives $f^{*'}(1)=\alpha$; hence $J_n(0)\sim\alpha^n$, and [6(a),6(b)] $\mu=\alpha$. Again, we see that, using forward coupling, we move in a very special direction in function space [13(b)]. Although the forward coupling is easy to work with, it is not generic.

B. Fluctuations and coherence length

Consider again the golden-mean path for the linear-coupled sine-map system. Figure 9 shows the spatial "landscape" of the phase at a particular time $n\gg 1$, for $K=1.1$ and for two J values, $J=0.1$ and 0.0015. The two landscapes are quite different; while coherent regions are clearly present at $J=0.1$, such regions are *not* observed at $J=0.0015$. This is an indication that the coherence length ξ decreases with decreasing J. More precisely, since $c_n(\mathbf{r})$ is the second spatial derivative, a rescaling of the spatial variable by $\sqrt{J}$ removes the J dependence in (2.1). Assuming that ξ is the only important length scale, one must have

$$\xi\sim\sqrt{J}\ . \tag{4.16}$$

Moreover, ξ is observed to increase as K decreases towards $K=K_c=1$, where the landscape becomes flat: $x_n(\mathbf{r})=x_n$ with $\xi=\infty$. By the renormalization-group analysis in Sec. IV A, we have the conjecture

$$\xi(J,K)=\xi(J/\alpha^2,(K-1)/\alpha^2)\ , \tag{4.17}$$

with the solution

$$\xi(J,K)=\xi(J/(K-1)^{\beta})\ , \tag{4.18}$$

where $\beta=1$. By (4.16),

$$\xi(J,K)\sim[J/(K-1)^{\beta}]^{1/2}\ . \tag{4.19}$$

The renormalization-group result for the forward coupling is obtained by replacing J/α^2 with $J/(1/R_g)=JR_g$. Then the exponent β is determined by $R_g\alpha^{2\beta}=1$, i.e., $\beta=-\ln R_g/(2\ln|\alpha|)=1/[2x(1)]=0.948\ldots$ which differs only slightly from the linear-coupling value $\beta=1$. The difference is more clear for coupled logistic maps. Here the eigenvalue $\mu=2$ for the forward coupling differs noticeably from the generic linear-coupling eigenvalue $\mu=\alpha$. The relevant eigenvalue for the K direction is $\delta=4.699\ldots$, so we have $\beta=\ln 2/\ln\delta=0.458\ldots$ for the forward coupling, while $\beta=\ln|\alpha|/\ln\delta=0.584\ldots$ for the (generic) linear coupling.

One way to measure the characteristic length ξ for the onset of spatiotemporal intermittency is through an equal-time two-point correlation function. However, above the onset of spatiotemporal intermittency, there persist highly active (turbulent) domain boundaries enclosing the coherent (laminar) regions. These macroscopic patterns have a substantial effect on the correlation function and it is very difficult to obtain a clean exponential decay.

Other ways to find ξ exist [9]. Here we shall take an approach based on a direct study of the phase fluctuations $y_n(\mathbf{r})$ [Eq. (2.6)] [10]. In addition to the distribution $D(y)$ of these fluctuations with width w [Eq. (3.30)], consider the distributions in space and time of the first and second "derivatives" [7], i.e., the distribution $D(\delta)$ of "gradients"

$$\delta_n(\mathbf{r},\mathbf{r}')\equiv|x_n(\mathbf{r})-x_n(\mathbf{r}')|\ , \tag{4.20}$$

between neighboring sites, with width

$$\Delta\equiv\{\ll[\delta_n(\mathbf{r},\mathbf{r}')]^2\gg\}^{1/2}\ , \tag{4.21}$$

and the distribution $D(c)$ of "curvatures" $c_n(\mathbf{r})$ [cf. (2.2)] with width

$$\kappa\equiv\{\ll[c_n(\mathbf{r})]^2\gg\}^{1/2}\ . \tag{4.22}$$

The widths w, Δ, and κ are all found to be *independent* of the random initial conditions. We shall see that the widths w, Δ, and κ are essential ingredients in the identification of a coherence length.

Figure 10(a) shows κ/Δ as a function of $1/\sqrt{J}$ for various values of K. Similar curves are found for Δ/w. At a certain K-dependent J value, $J=J_c(K)$, a crossover is observed, separating two distinct regions: (i) $J>J_c(K)$, where κ/Δ and Δ/w both are proportional to $1/\sqrt{J}$; (ii) $J<J_c(K)$, where Δ/r and r/w are constant. The crossover at $J=J_c(K)$ originates from the point where the coherence length ξ becomes 1 (the lattice unit). When $\xi\gg 1$, the spatial variation is "smooth," and the existence of a coherence length suggests the relation (by dimensional analysis)

$$\kappa\sim\Delta/\xi\sim w/\xi^2\ . \tag{4.23}$$

From (4.23) it follows that the two ratios κ/Δ and Δ/w both scale like ξ^{-1}, in accordance with (4.16). Since w is not affected by spatial rescaling, (4.23) also implies that $\Delta\sim 1/\sqrt{J}$ and $\kappa\sim 1/J[\xi\gg 1]$. Numerical simulations confirm this behavior (Fig. 11).

For $\xi\ll 1$, w, Δ, and κ are all of the same magnitude, and their values are much larger than 1. Assuming that the sine term in (2.3) behaves as a random variable with amplitude $1/\sqrt{2}$, we have at time n $[x_0(\mathbf{r})\approx 0]$

$$y_n(\mathbf{r})=\frac{K}{2\pi}\sum_{m=0}^{n-1}\zeta_m(\mathbf{r})+J\sum_{m=0}^{n-1}c_m(\mathbf{r})\ , \tag{4.24}$$

where $\zeta_n(\mathbf{r})$ is random (with amplitude $1/\sqrt{2}$). Since the

sum of n random numbers has width $\sqrt{n}$, w will be of order $K\sqrt{n}$. Therefore $\kappa \sim K\sqrt{n}$, and the last term in (4.24) is of order $JnK\sqrt{n}$. The dynamics stabilizes when all terms are of the same order, i.e., when $n \sim 1/J$. Thus

$$w \sim K/\sqrt{J}, \quad \Delta \sim K/\sqrt{J}, \quad \kappa \sim K/\sqrt{J} \quad (\xi \ll 1) . \tag{4.25}$$

The interpretation of $J_c(K)$ as the value for which ξ equals 1, suggests that ξ is a function of $J/J_c(K)$, or since $\xi \sim \sqrt{J}$,

$$\xi \sim \sqrt{J/J_c(K)} . \tag{4.26}$$

By (4.19), (4.26) yields

$$J_c(K) \sim (K-1)^{\beta} . \tag{4.27}$$

Numerically, one finds $\beta = 1.2 \pm 0.2$. This value should be compared with the unit value of β obtained by renormalization-group analysis.

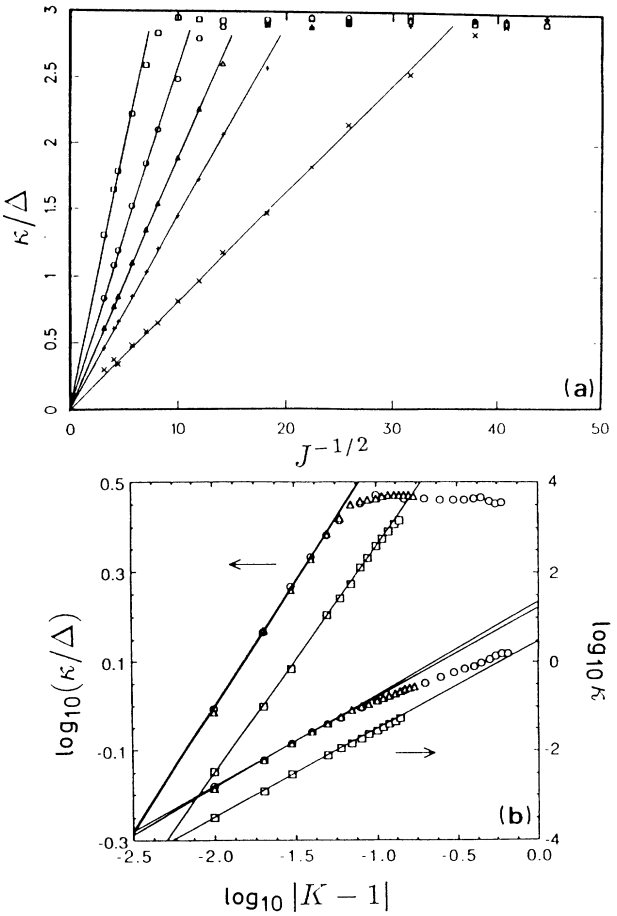

FIG. 10. (a) The ratio κ/Δ obtained for $R = R_g$ and plotted vs $1/\sqrt{J}$ for various values of K. From left to right, $K = 1.10$, 1.05, 1.03, 1.02, and 1.01. (b) κ/Δ and κ for $R = R_g$ (○) and $R = R(2)$ (△), and for the sine-cubed map at $R = R_g$ (□), and plotted $K-1$ (log-log) for $J = 0.01$. Below the crossover, the slopes are found to be 0.56, 0.56, and 0.51 for κ/Δ (left curves), while the slopes for κ (right curves) are found to be 2.01, 2.10, and 1.98.

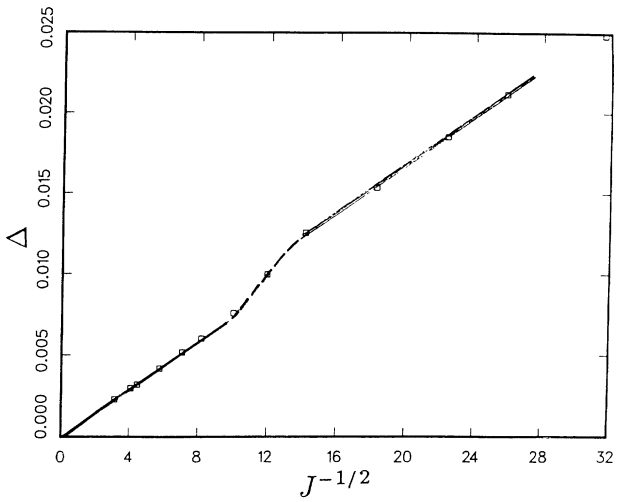

FIG. 11. The width Δ of the gradient distribution $D(\delta)$, obtained for $K = 1.03$ and $R = R_g$. For both regimes ($\xi \gg 1$ and $\xi \ll 1$) $\xi \sim 1/\sqrt{J}$. The crossover from one regime to the other can, however, easily be detected as a disruption of the linear behavior.

More accurately, one can directly find the K dependence of ξ, e.g., by determining κ/Δ as a function of K. By (4.19) and (4.23), $\kappa/\Delta \sim (K-1)^{\beta/2}$. Figure 10(b) shows the result for $J = 0.01$. A least-squares fit yields $\beta/2 = 0.56$. Since our accuracy decreases close to $K = 1$, we cannot exclude the possibility that β is eventually given by the unit renormalization-group value. Also shown in Fig. 10(b) is κ for various values of K (for fixed $J = 0.01$). The points at low values of $K-1$ follow a straight line with slope $\gamma \simeq 2.01$. From (4.19) and (4.23), the following scaling behavior of w, Δ, and κ is now obtained:

$$w \sim (K-1)^{\gamma-\beta}, \quad \Delta \sim (K-1)^{\gamma-(\beta/2)}/\sqrt{J} , \quad \kappa \sim (K-1)^{\gamma}/J \quad (\xi \gg 1) . \tag{4.28}$$

To examine the universality of the exponents β and γ, we (i) follow another route with rotation number $R = R(2) = \sqrt{2} - 1$ and (ii) use another circle map $f = f_a$, where

$$f_a[x_n(\mathbf{r})] = x_n(\mathbf{r}) + \Omega - \frac{K}{2\pi}\{\sin[2\pi x_n(\mathbf{r})] + a \sin^3[2\pi x_n(\mathbf{r})]\} , \tag{4.29}$$

with $\alpha = -\frac{1}{2}$. The results are shown in Fig. 10(b). The exponents obtained are identical to the golden-mean exponents within an accuracy of 5%.

For an experimental system, the method to measure a coherence length from spatial-derivative plots can be used when an underlying lattice is determined by a basic length scale and the geometry. For the thin fluid layer in a container, the basic length scale is the wavelength, for Rayleigh-Bénard convection, it is the roll size. For

Taylor-Couette flows, the basic length is the distance between the cylinders (or more precisely the size of the spirals). Having identified the basic length scale, and thereby the lattice unit, it is clear how to proceed. The basic length scale should be observed at the onset of spatiotemporal intermittency since it generally changes with the nonlinearity. Typically, this variation is small.

C. Lyapunov exponent

Next consider a perturbation $\delta\vec{x}_0$ of the system in its stationary state ($n \gg 1$). The Lyapunov exponent λ expresses how fast perturbations grow in time,

$$\lambda \equiv \lim_{t\to\infty} t^{-1} \lim_{\delta x_0 \to 0} \ln\left[\frac{\delta x_t}{\delta x_0}\right], \tag{4.30}$$

where δx_t is the length of the perturbation $\delta\vec{x}_t$ after a time t. Hence λ represents a natural frequency of the system. However, from the identification of $x_{n+1}(\mathbf{r}) - x_n(\mathbf{r})$ as a time derivative, dimensional analysis of (2.1) yields a natural frequency ω given by $\omega w \sim J\kappa$, and the relation (4.23) leads to $\omega \sim J/\xi^2 = J_c$ [for $\xi > 1$; cf. (4.26)]. We are therefore led to the conjecture $\lambda \sim J_c$, i.e.,

$$\lambda \sim (K-1)^{\beta}, \tag{4.31}$$

which contains no J dependence.

We notice that for both the sine map and the logistic map, the behavior (4.31) for λ, given by the (linear-coupling) renormalization-group value of β, differs from the behavior found for a single map, where β has the smaller forward-coupling value [23,24]. Naively, this seems to contradict the "missing" J dependence in (4.31), since $J=0$ gives the single-map result. It is, however, important to remember that (4.31) is only valid in the regime $J > J_c(K)$, and one cannot take the limit $J \to 0$ for fixed K.

The conjectured scaling behavior for λ can be tested by perturbing the system by a small value ϵ at *one* site, i.e., $\delta x_0 = \epsilon$, and then follow the temporal development of δx_t in the time regime where δx_t still grows. Numerical results obtained for $1.01 \le K \le 1.5$ and $0.001 \le J \le 0.1$ show no significant dependence of λ on J, and are consistent with the conjectured K dependence [25].

The scaling (4.3) for the Lyapunov exponent λ leads to a scaling result for the width w of the phase fluctuations. This is most clearly illustrated for $J \simeq 0$. For any perturbation δx from the homogeneous state x_0, iterations eventually increase (or decrease) the perturbation to w, i.e., for sufficiently large N,

$$f^N(x_0 + \delta x) = f^N(x_0) + w . \tag{4.32}$$

To second order,

$$f^N(x_0+\delta x) = f^N(x_0) + (f^N)'(x_0)\delta x + \tfrac{1}{2}(f^N)''(x_0)\delta x^2 . \tag{4.33}$$

In particular, $\delta x = w$ yields

$$w = 2\frac{1-(f^N)'(x_0)}{(f^N)''(x_0)} \simeq \frac{1-\left[\prod_{i=0}^{N-1} f'(x_i)\right]^{-1}}{N\phi(\Omega,K)}, \tag{4.34}$$

where

$$\phi(\Omega,K) = \lim_{N\to\infty} \frac{1}{N} \sum_{i=0}^{N-1} [-f''(x_1)/2f'(x_i)] . \tag{4.35}$$

Since $\prod_{i=0}^{N-1} f'(x_i) \sim e^{N\lambda}$, we have

$$w \sim \lambda \sim (K-1)^{\beta} . \tag{4.36}$$

Hence, by (4.28),

$$\gamma = 2\beta , \tag{4.37}$$

in agreement with numerical results (Fig. 10).

V. PERCOLATION METHODS FOR SPATIOTEMPORAL CHAOS

A. Laminar and turbulent regions

In fluid dynamics, spatiotemporal intermittency is the coexistence of a laminar and a turbulent phase in space and time. One example is the flow of water down a pipe. The first experiment on this phenomenon was conducted by Reynolds. By monitoring the flow using a dye he was able to distinguish a laminar and a turbulent phase in the fluid motion as well as their time evolution [26]. One simple (although arbitrary) way to make a distinction between laminar and turbulent regions in coupled dynamical systems is by choosing a cutoff. Recently, this type of phase separation has been studied quantitatively, both in model systems [8,27] and in actual experiments [2].

Consider the absolute value of the gradients $\delta_n(\mathbf{r},\mathbf{r}')$ [Eq. (4.20)] between neighboring lattice points $\mathbf{r}$ and $\mathbf{r}'$. This is a quantity analogous to the temperature fluctuations in Rayleigh-Bénard convection experiments or to the velocity fluctuations in a pipe flow. In order to discern the turbulent from the laminar, an arbitrary cutoff α is introduced. If the difference $d_n(\mathbf{r},\mathbf{r}')$ is larger than the chosen cutoff, the corresponding bond is considered turbulent; otherwise it is laminar. We refer to the resulting clusters (groups of connected turbulent bonds) as *turbulent bursts.* The *turbulence strength* p is then defined as the ratio of turbulent cluster sites over the total number of sites. Having developed a systematic procedure to identify the turbulent bursts, we can pursue the standard statistical treatment, widely used in the study of critical phenomena and percolation theory. The goal is to characterize the spatiotemporal regime in terms of scaling exponents and, if possible, identify the appropriate universality classes.

B. Spatiotemporal chaos and bond percolation

Based on the above identification of turbulent clusters, we define n_s as the distribution of turbulent bursts of size s. Consider again the coupled sine-map lattice. For $\alpha = 0.5$ and $J = 0.01$ we examine the behavior of n_s along three different paths: (i) the golden-mean path $K = K(\Omega)$, for which $R(\Omega, K(\Omega)) = R_g$; (ii) $\Omega = 0.5$; (iii) $\Omega = 0.635$.

Figure 12 shows the results from a statistical analysis of the turbulent bursts on a 30×30 lattice over 24 000

successive time steps (considered as a statistical ensemble) after the system is let to relax through 1000 iterations. For values of the nonlinearity K close to 1, the turbulent bursts are sparse and fragmented; n_s follows a power law up to a characteristic size s_0 for then to fall off exponentially [Fig. 12(a)]. As we drive the system harder, increasing K, the characteristic size s_0 becomes larger. At a certain critical value of K, K_c, corresponding to a critical value for p, $p_c \equiv p(K_c)$, the exponential tail is completely suppressed [Fig. 12(b)]. This behavior can be summarized in an expression similar to the one appearing in percolation theory:

$$n_s \propto s^{-\tau} \exp(-s/s_0) \ . \tag{5.1}$$

The exponent τ is found to be "universal"; for all cases, $\tau \simeq 1.73 \pm 0.08$. Moreover, while K_c differs from case to case [from $K_c \simeq 1.89$ in (i) to $K_c \simeq 2.28$ in (ii)], p_c remains constant, $p_c = 0.465 \pm 0.005$. Also, the values of τ and p_c do not change when we increase the cutoff or the coupling constant, e.g., (iv) $\alpha = 1.0$, $J = 0.01$, $\Omega = 0.5$; (v) $\alpha = 0.5$, $J = 0.1$, $\Omega = 0.5$.

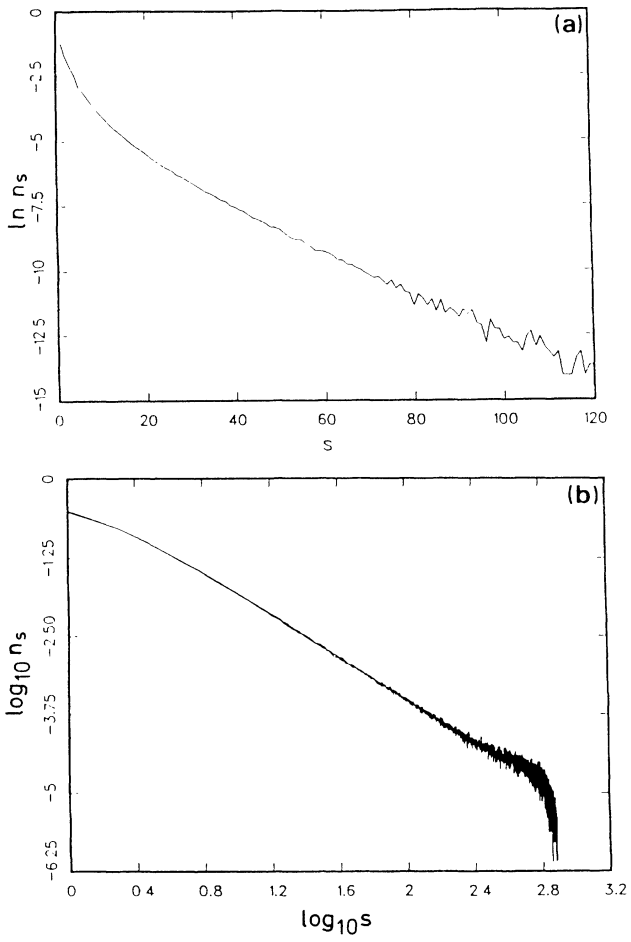

FIG. 12. n_s for a 30×30 system at $J = 0.01$. (a) on (i) at $K = 1.55 < K_c$, semi-logarithmic plot; (b) on (i) at $K = K_c = 1.89$, (ii) at $K = K_c = 2.28$, (iii) at $K = K_c = 1.95$, double-logarithmic plot.

While the value found for the turbulence strength is comparable with the value for bond percolation on a square lattice, $p_c = \frac{1}{2}$, the value of τ is lower than the percolation value $\tau = 187/91 = 2.0549\ldots$. However, for a 30×30 system finite-size effects are substantial. Repeating the calculation of p_c and τ for a 100×100 system along path (ii) $\Omega = 0.5$ yields $p_c = 0.497 \pm 0.005$, and $\tau = 2.0 \pm 0.1$, in accordance with bond percolation. Still, finite-size corrections are noticeable for crossover exponents such as the scaling exponent σ, associated with the characteristic length s_0 [cf. (5.1)],

$$s_0 \propto |p - p_c|^{-1/\sigma} \ . \tag{5.2}$$

By plotting $\ln(s^{\tau} n_s)$ vs s, $1/s_0$ is determined as the (absolute) slope. Repeating the procedure for different p values, s_0 is found as a function of p, and σ can be determined. Using $p_c = 0.50 \pm 0.01$ gives $\sigma = 0.46 \pm 0.05$. This value for σ is slightly larger than the theoretical percolation value $\sigma = \frac{36}{91} = 0.3956\ldots$, but not different from the value obtained numerically for (bond) percolation on a 100×100 lattice ($p_c = 0.49 \pm 0.01$, $\tau = 2.0 \pm 0.1$, and $\sigma = 0.46 \pm 0.05$).

From the analysis above two main conclusions are derived. The first is that the scaling exponents for the distribution n_s, derived for the sine-map system (2.1)–(2.3), seem to fall within the universality class of percolation when $\alpha \sim 1$ (see below) [8(c)]. The second is that finite-size effects are important, and unless one works with large systems, significant deviations from (infinite-size) percolation exponents are to be expected. Both conclusions are particularly relevant for experiments [2], where the system size generally is relatively small and the cutoff α is chosen of the order of a typical oscillation amplitude.

How do we account for the appearance of the percolation universality class? From our discussion in Sec. IV it became clear that the coherence length ξ characterizing the patterns decreases fast with increasing K or decreasing J. For example, for a fixed J value, $J = 0.01$, K becomes comparable to the lattice spacing already for a value of $K \sim 1.1$. Comparing this value to the values of K_c found above ($K_c \geq 1.89$), we find that even nearest neighbors are uncorrelated. We emphasize that this does not necessarily mean that each gradient takes on a random value as is the case with bond percolation. In fact, real-time observation reveals a dynamics much richer than that of random noise [28].

C. Spatiotemporal intermittency

To quantify the "static" properties of the sine-map system, we consider the normalized distribution $D(\delta)$ of the gradients $\delta_n(\mathbf{r}, \mathbf{r}')$. In Fig. 13 we show a number of distributions obtained for the golden-mean path and for the $\Omega = \frac{1}{2}$ path ($J = 0.01$). Fitting with a Gaussian distribution seems to give a reasonable approximation, but there are observable deviations. Periodic fluctuations are superimposed on all the distributions and show the tendency of the system to synchronize its phases. The main period both for the irrational path as well as the mode-

locked path is 2π. Synchronization of phases differing by one, two, and three cycles is clearly seen, even differences of four or five cycles are observable, although much reduced. For the $\Omega=\frac{1}{2}$ path, also the π period is apparent.

Neglecting the "modulation" on the distribution $D(\delta)$ when $\xi<1$, we have approximately

$$D(\delta;\Omega,K,J)\simeq\frac{1}{\Delta}\phi\left[\frac{\delta}{\Delta}\right], \tag{5.3}$$

where $\Delta=\Delta(\Omega,K,J)$ is the width of $D(\delta)$ [Eq. (4.21)] and $\phi(z)$ is the Gaussian distribution

$$\phi(z)\equiv\frac{2}{\sqrt{2\pi}}\exp\left[-\frac{z^2}{2}\right]\quad(z\geq 0)\ . \tag{5.4}$$

Based on this approximation, we have for the turbulence strength p,

$$p=\int_{\delta=\alpha}^{\infty}D(\delta)d\delta=\int_{z=\alpha/\Delta}^{\infty}\phi(z)dz\ . \tag{5.5}$$

Thus, to the extent that the approximation (5.3) is valid, we are able to reduce the initial $(\alpha;\Omega,K,J)$ dependence of p,

$$p(\alpha;\Omega,K,J)=\Phi(\alpha/\Delta(\Omega,K,J))\ , \tag{5.6}$$

where

$$\Phi(u)\equiv\int_u^{\infty}\phi(z)dz=\int_u^{\infty}\frac{2}{\sqrt{2\pi}}\exp\left[-\frac{z^2}{2}\right]dz\ . \tag{5.7}$$

Then, in the regime where $\xi<1$, all points $[p(\alpha;\Omega,K,J);\alpha/\Delta(\Omega,K,J)]$ should collapse onto the same curve. Figure 14(a) shows that these points, determined for different cutoffs at different configurational points, approximately all lie on the same curve.

Consider next the $\xi>1$ regime. In Sec. IV we have seen that this regime is characterized by a clear change of the scaling behavior characterizing w, Δ, and κ. A corresponding crossover to the $\xi>1$ regime is, however, very difficult to observe in the power-law behavior of n_s. To ensure that we are in the spatiotemporal intermittent regime, α must be reduced by one order of magnitude. This makes it excessively difficult for one to tell whether a developing trend constitutes a new power-law behavior

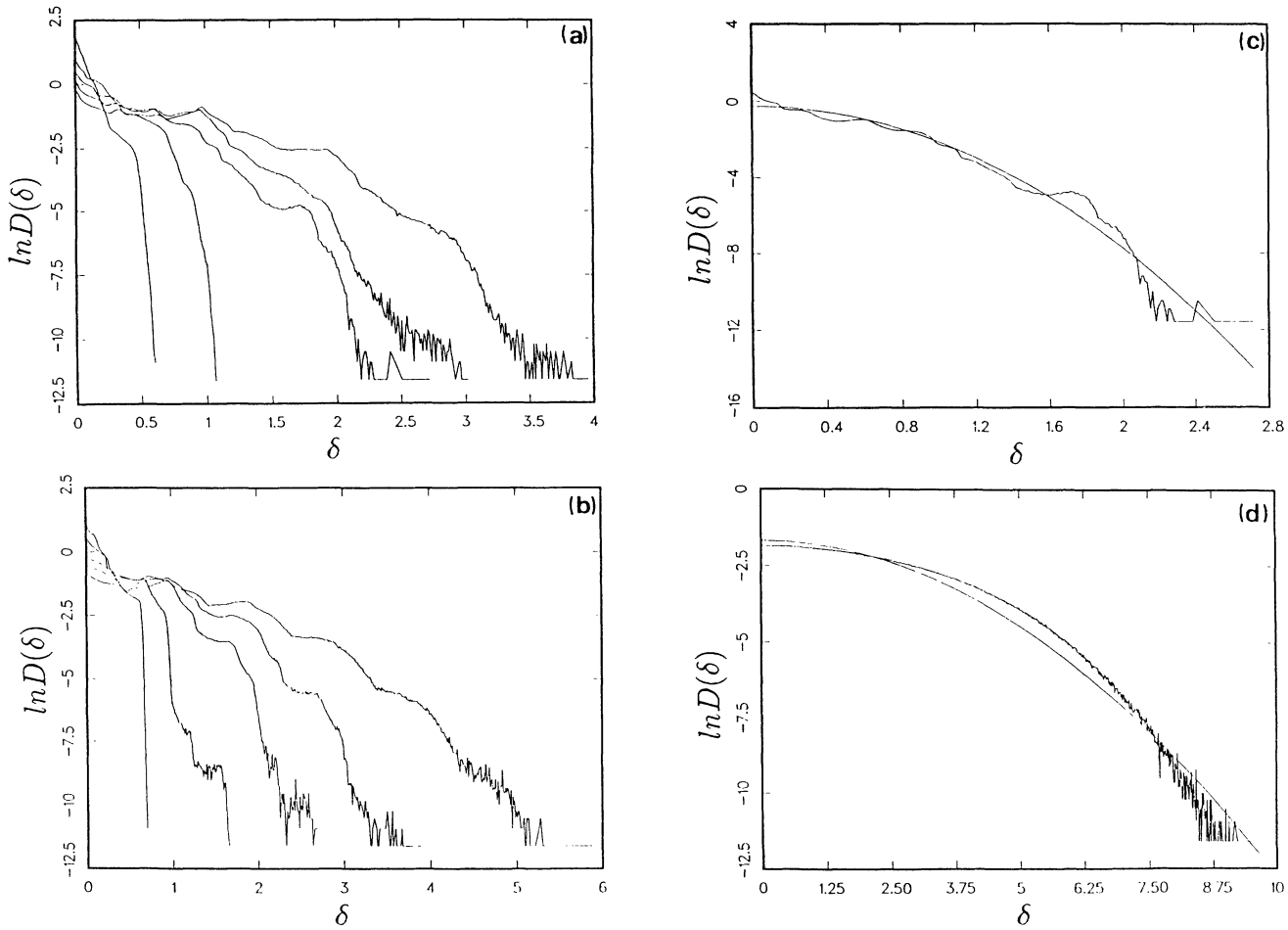

FIG. 13. Logarithmic plots of the normalized distribution $D(\delta)$ of gradients δ. (a) for the golden-mean path at $J=0.01$, and different K values (from left to right): 1.20, 1.40, 1.70, 1.89, and 2.00. (b) for the $\Omega=\frac{1}{2}$ path at $J=0.01$; K values from left to right: 2.00, 2.10, 2.20, 2.40, and 2.80. (c) and (d) Comparison with corresponding Gaussian distributions (determined by least-squares fitting). (c) $K=1.70$ and $J=0.01$, on the golden-mean path. (d) $K=12.0$, $J=0.1$, and $\Omega=\frac{1}{2}$.

or it is just an effect of the modulations on the distribution $D(\delta)$.

Another noticeable difference in the $\xi > 1$ regime is the dependence of p_c on α. p_c tends to decrease with decreasing α. For instance, when $\alpha = 0.15$ the corresponding p_c value is $p_c \simeq 0.27$. We can qualitatively account for this dependence by looking at the distributions $D(\delta)$. When α is tuned to small values ~ 0.1, small δ values come into play, and the deviations from the Gaussian distribution become important [remember that the peak at $\delta = 0$ (Fig. 13) is greatly suppressed by the logarithmic scale]. Another way to demonstrate the disparity from Gaussian behavior in this regime is by direct numerical testing of the rescaling hypothesis (5.6). In Fig. 14(b) p is shown as a function of α/Δ ($J = 0.01$). The deviations for intermediate values of α/Δ demonstrate the breakdown of the rescaling assumption (the convergence of the data to 1 in the limit of small α/Δ follows since any normalized distribution gives $p = 1$ for $\alpha = 0$).

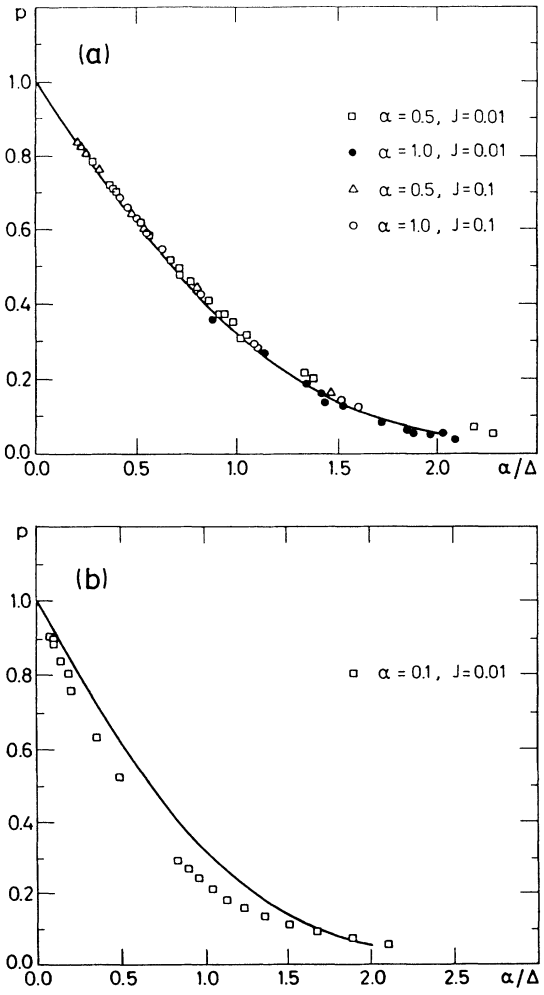

FIG. 14. (a) p vs α/Δ for different configurational points $(\alpha;\Omega,K,J)$ inside the $\xi < 1$ regime. The solid line depicts the $\Phi(\alpha/\Delta)$ function. (b) p vs α/Δ for configurational points in the $\xi \sim 1$ regime.

The analysis has shown the existence of two regimes: One corresponds to $\xi < 1$. In this regime a universal scaling behavior is observed, where the exponents τ and σ as well as p_c are found identical to those of bond percolation. For this regime, p is the single relevant parameter. In contrast to the $\xi < 1$ regime (where p_c remains fixed), p_c decreases as we get closer to the onset of spatiotemporal intermittency. It is, however, very difficult to obtain a clear power-law behavior for the cluster size distribution n_s in the regime corresponding to $\xi > 1$.

VI. CONCLUSIONS

We have studied coupled-map lattices in the transition regime to spatiotemporal intermittency and chaos. We have shown that, although forward coupling is easy to work with, it is nongeneric, and a linear coupling term must be considered in general. In this case, the breakdown of a homogeneous periodic state results in patterns with short wavelengths; however, the wavelength increases with the period. In particular, we have derived the stability conditions for the checkerboard state, and discussed its dependence on initial conditions in terms of a nucleation picture. Along the period-doubling route to chaos, we have calculated the phase fluctuation width, which is found to increase square-root-like at the first formation of checkerboards. Below the transition to spatiotemporal chaos, the width in general depends on the initial conditions (which is not the case above).

Following a quasiperiodic path leads to spatiotemporal intermittency. At the onset of chaos, patterns emerge with a characteristic coherence length. For the golden-mean path, the scaling properties for the coherence length ξ are found by renormalization-group analysis. The results are tested numerically, using a method based on the distributions of the phase fluctuations and their derivatives. The relation between the coherence length and the Lyapunov exponent is discussed.

Finally, we have examined the use of percolation methods in the study of spatiotemporal intermittency. Usual percolation exponents are obtained in the small-ξ regime. We have seen that finite-size effects are substantial and cannot be ignored. This is of special importance in experimental systems where it is very difficult to work with variable sizes. Another point is that the study of the $\xi > 1$ regime requires tuning the system very close to the onset of spatiotemporal intermittency. This tuning cannot be done after a cutoff is fixed because the transition point is not known beforehand, neither is the appropriate range of values for the $\xi > 1$ regime. In that respect the procedure described in Sec. IV offers an alternative way for finding the $\xi > 1$ regime. Then, if wanted, a cutoff can be chosen appropriately.

ACKNOWLEDGMENTS

We are very grateful to Tomas Bohr for stimulating discussions and to Greg Huber for valuable comments and for carrying out numerical simulations. Also, we are indebted to George Schmidt for inspiring conversations at the Aspen Center of Physics, where the renormalization-group analysis was initiated.

[1] A. Pocheau, V. Croquette, and P. Le Gal, Phys. Rev. Lett. **55**, 1094 (1985).

[2] P. Bergé, Nucl. Phys. B **2**, 247 (1987); S. Ciliberto and P. Bigazzi, Phys. Rev. Lett. **60**, 286 (1988); F. Daviaud, M. Dubois, and P. Bergé, Europhys. Lett. **9**, 441 (1989).

[3] N. B. Tuffilaro, R. Ramshankar, and J. P. Gollub, Phys. Rev. Lett. **62**, 422 (1989).

[4] G. Zocchi, S. Gross, and A. Libchaber, in *Random Fluctuations and Pattern Growth: Experiments and Models,* edited by H. E. Stanley and N. Ostrowsky (Kluwer, Dordrecht, 1988).

[5] J. Stavans, F. Heslot, and A. Libchaber, Phys. Rev. Lett. **55**, 596 (1985).

[6] (a) I. Waller and R. Kapral, Phys. Rev. A **30**, 2047 (1984); (b) R. Kapral, *ibid.* **31**, 3868 (1985); (c) G.-L. Oppo and R. Kapral, *ibid.* **36**, 5820 (1987).

[7] K. Kaneko, Prog. Theor. Phys. **72** (1984); **74**, 1033 (1985); Physica D **37**, 60 (1989); J. Crutchfield and K. Kaneko, in *Directions in Chaos,* edited by Hao Bai-Lin (World Scientific, Singapore, 1987), Vol. 1.

[8] (a) H. Chaté and P. Manneville, Europhys. Lett. **6**, 591 (1988); (b) Physica D **32**, 409 (1988); (c) Phys. Rev. A **38**, 4351 (1988).

[9] T. Bohr, G. Grinstein, Yu He, and C. Jayaprakash, Phys. Rev. Lett. **58**, 2155 (1987); T. Bohr and O. B. Christensen, *ibid.* **63**, 2161 (1989).

[10] D. Stassinopoulos, G. Huber, and P. Alstrøm, Phys. Rev. Lett. **64**, 3007 (1990).

[11] See, e.g., M. H. Jensen, P. Bak, and T. Bohr, Phys. Rev. A **30**, 1960 (1984).

[12] M. J. Feigenbaum, J. Stat. Phys. **19**, 25 (1978); **21**, 669 (1979); see, e.g., P. Collet and J. P. Eckmann, *Iterated Maps on the Interval as Dynamical Systems* (Birkhaüser, Boston, 1980).

[13] (a) S. P. Kuznetsov and A. S. Pikovsky, Physica D **19**, 384 (1986); (b) S. P. Kuznetsov, Radiofizika **29**, 887 (1986).

[14] From (2.3) with $\Omega=\frac{1}{2}$ it is straightforwardly seen that this orbit is independent of K.

[15] This smoothing from a perturbed to a nearly homogeneous state was noted in Ref. [6(b)].

[16] A thorough analysis of a similar nucleation process in a cubic-map lattice can be found in Ref. [6(c)].

[17] The nucleation process is here described in terms of the nucleation time. For the cubic-map lattice a quantitative stability analysis in terms of the nucleation radius, including its dependence on the coupling constant, is given in Ref. [6(b)].

[18] In Fig. 6 the K dependence of $\tau^{(s)}$ is neglected close to K_1. The smoothing effect is expected to depend primarily on the diffusive term and not on the nonlinear term.

[19] We cannot increase the heat excessively: above $h\sim 0.33$ the system tends to stabilize in (more "energetic") non-checkerboard states.

[20] (a) S. J. Shenker, Physica D **5**, 405 (1982); (b) M. J. Feigenbaum, L. P. Kadanoff, and S. J. Shenker, *ibid.* **5**, 370 (1982); (c) S. Ostlund, D. Rand, J. Sethna, and E. Siggia, *ibid.* **8**, 303 (1983).

[21] P. Alstrøm, M. T. Levinsen, and R. R. Rasmussen, Physica D **26**, 336 (1987).

[22] H. Kook, F. H. Ling, and G. Schmidt, Phys. Rev. A **43**, 2700 (1991).

[23] B. Shraiman, C. E. Waine, and P. C. Martin, Phys. Rev. Lett. **46**, 935 (1981).

[24] M. H. Jensen and I. Procaccia, Phys. Rev. A **32**, 1225 (1985).

[25] Detailed analysis of Lyapunov exponents in coupled-map lattices has been carried out by K. Kaneko [Physica D **23**, 436 (1986); **34**, 1 (1989)], F. Kaspar and H. G. Schuster [Phys. Lett. **113A**, 451 (1986)], and T. Bohr and O. B. Christensen (Ref. [9]). From our results for the Lyapunov exponent, we cannot carry out a similar analysis. We are, however, able to exclude the possibility that $\lambda\sim\xi^{-1}$.

[26] O. Reynolds, Philos. Trans. R. Soc. London **174**, 935 (1883); *Papers on Mechanical and Physical Subjects* (Cambridge University Press, Cambridge, England, 1901), Vol. II, p. 51.

[27] H. Chaté and P. Manneville, Phys. Rev. Lett. **58**, 112 (1987); Phys. Rev. A **38**, 4351 (1988).

[28] As a comment on the question of why percolation exponents are found, although there are significant differences between the sine-map system and bond percolation, we refer to the *correlated bond-percolation model* [A. Coniglio, J. Phys. A **8**, 1773 (1975)]. This model describes a process for growing bond-percolation clusters on spanning Ising-spin clusters, and is known to produce the percolation exponents for any finite correlation length of the underlying clusters. It gives, however, different values for the percolation threshold p_c.

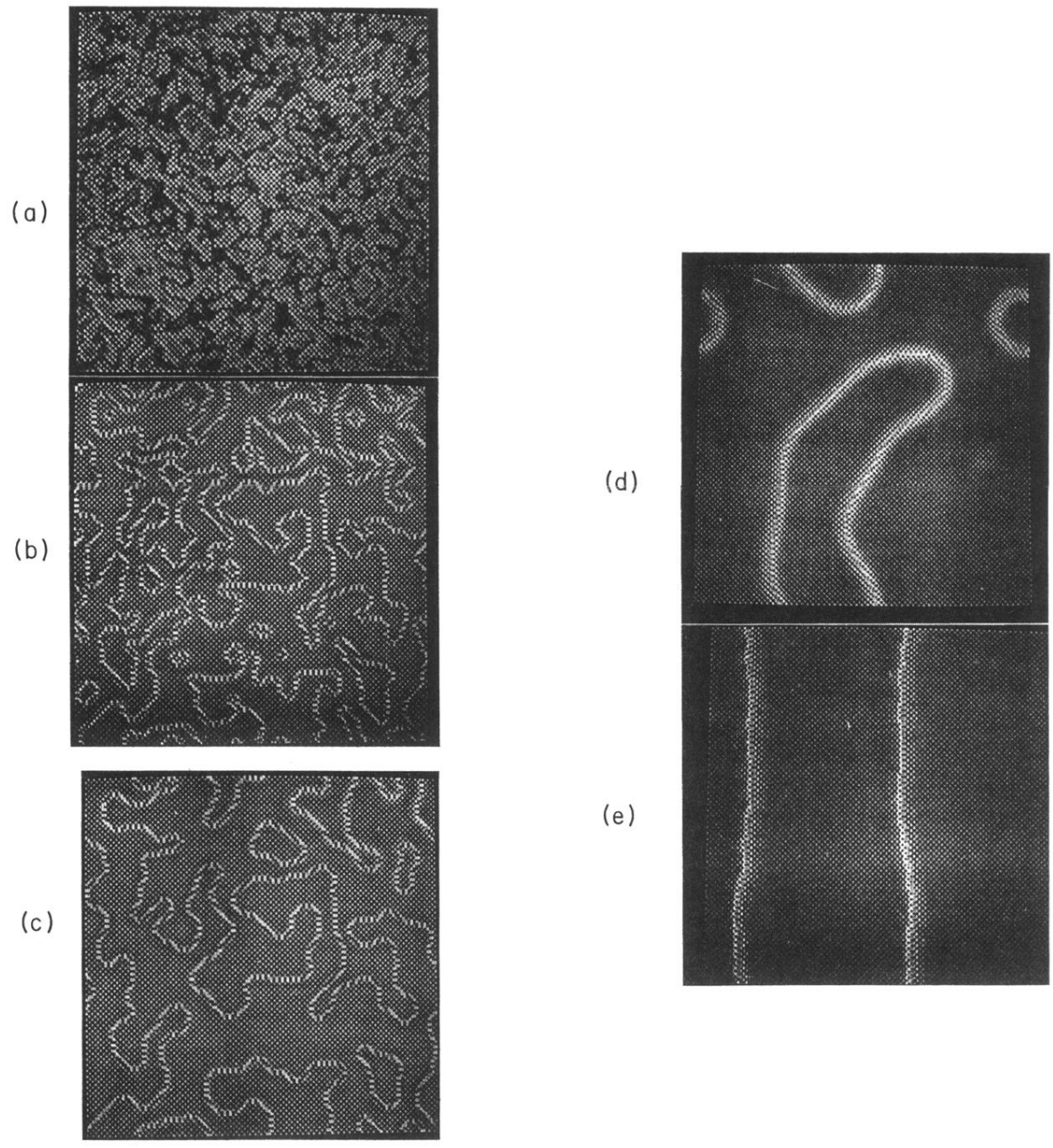

FIG. 3. (a)–(c) Checkerboard evolution for a 128×128 system at $K=1.380$ and $J=0.01$. (a) 150 time steps. (b) 500 time steps. (c) 2000 time steps. (d)–(e) Two distinct checkerboard states for a 128×128 system at $K=1.025$ and $J=0.1$. (d) 3000 iterations. The loops will eventually disappear after $\sim70\,000$ iterations. (e) The same system started from different initial conditions after 100 000 iterations. The domain walls will remain.

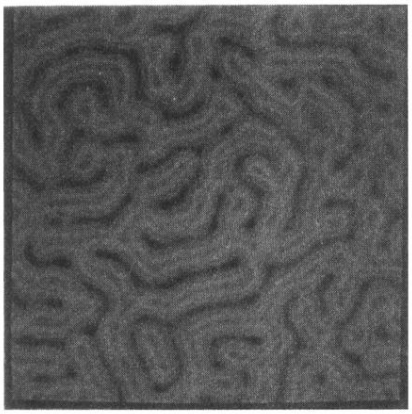

FIG. 4. A snapshot for a 128×128 system at $K = 1.048\,95$ and $J = 0.1$ along the $\frac{13}{21}$ Arnold tongue.

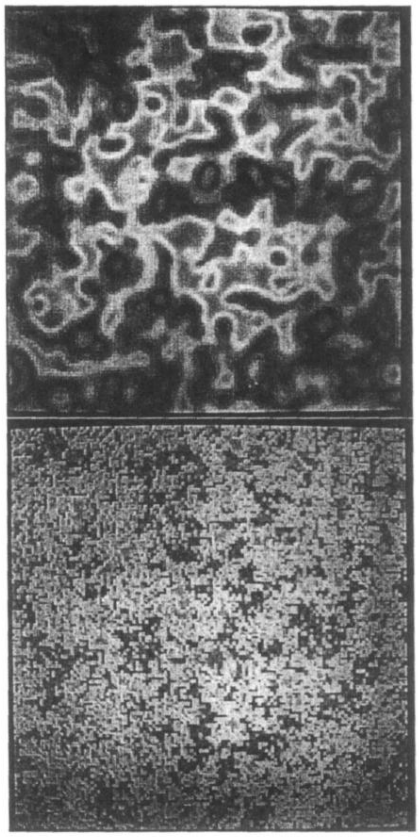

FIG. 9. Two typical spatial patterns above the onset of chaos (system size 128×128). $K = 1.1$ and (a) $J = 0.1$, (b) $J = 0.0015$. The value of Ω is chosen such that the rotation number equals the golden mean R_g.